

DIFFUSION AND RELATED PHENOMENA IN BULK NANOSTRUCTURED MATERIALS

M. D. Baró¹, Yu. R. Kolobov², I. A. Ovid'ko³, H.-E. Schaefer⁴, B.B. Straumal⁵,
R. Z. Valiev⁶, I.V. Alexandrov⁶, M. Ivanov², K. Reimann⁴, A. B. Reizis³, S. Suriñash¹
and A.P. Zhilyaev^{1, 6}

¹ Universitat Autònoma de Barcelona, 08193 Bellaterra, Spain

² Institute of Strength Physics and Materials Science, Tomsk, Russia

³ Institute of Problems of Mechanical Engineering, St.-Petersburg, Russia

⁴ Universitaet Stuttgart, Institut fuer Theoretische und Angewandte Physik, 70550 Stuttgart, Germany

⁵ Institute of Solid State Physics, 142432 Chernogolovka, Moscow District, Russia

⁶ Institute for Physics of Advanced Materials, Ufa State Aviation Technical University, 450000 Ufa, Russia

Received: June 9, 2001; received in revised form: August 27, 2001

Abstract. The paper reviews results of experimental and theoretic studies of diffusion and related phenomena (grain growth, creeps, superplasticity) in bulk nanostructured materials. The particular attention is paid to the recent development in fabrication of bulk nanostructured materials and their microstructural characterization, evolution of bulk nanostructured materials during heating. Experimental study and theoretical modeling of grain boundary diffusion in bulk nanostructured materials are described. Related phenomena (grain growth, creep, superplasticity) in such materials and also ordering-reordering kinetics are presented.

CONTENTS

1. Introduction
2. Recent developments in fabrication of bulk nanostructured materials using severe plastic deformation
3. Thermal stability and microstructure evolution in severe plastic deformed (SPD) materials during annealing
4. The grain boundary diffusion in nanostructured materials
5. Theoretical modeling of grain boundary diffusion in bulk nanostructured materials
6. Related phenomena (grain boundary phase phenomena, superplasticity) in nanostructured materials
7. Ordering-reordering kinetics in Ni₃Al base alloys processed by ball milling
8. Concluding remarks

1. INTRODUCTION

Since the introduction of nanocrystalline materials and the progress in preparation techniques, many investigators have hoped to discover extraordinary

properties (physical and mechanical) in pure metals and alloys with nanocrystalline structure. This hope is broadly based on the fact that grain boundary (GB) related phenomena should effectively manifest themselves as grain size decreases to nanorange scale. Therefore, nanocrystals, materials with mean grain size of 100 nm and less, have recently become the subject of noteworthy interest. They demonstrated novel and often extraordinarily properties such as a decrease in the elastic moduli, decrease of Curie and Debye temperatures, enhanced diffusivity and improved magnetic properties [1]. With respect to mechanical properties e. g., high strength, wear resistance, ductility, high strain-rate superplasticity were observed in many experiments [2]. Recently *Nature* published the paper on finding of low temperature and/or high strain rate superplasticity in nanocrystalline metals and alloys [3]. These results have remarkable scientific value for materials science and allow developing of new technology for superplastic forming of complex shape components. It is supposed that such superplastic properties of nanocrystalline materials is due to abnormally high diffusivity and has been indi-

Corresponding author: A. P. Zhilyaev, e-mail: AlexZh@mail.rb.ru

rectly confirmed in some publications on diffusion measurements in nanocrystalline materials [4, 5]. Moreover, both high diffusivity and high strain rate superplasticity may be induced by the grain boundary phase transitions (see Chapter 6 of this review). Therefore, the application of the recently proposed GB phase diagrams will allow to explain the unusual properties of nanocrystalline materials and to develop the advanced nanocrystalline alloys with novel properties.

A comprehensive study of physical and mechanical properties has become possible as innovative methods such as severe plastic deformation (SPD) and ball-milled powders consolidation, were advanced. By these methods bulk nanostructured samples from pure metals, alloys and usually thought brittle intermetallics can be processed [6, 7]. However, nanostructured materials processed by different methods often differ drastically in properties in spite of the fact that they have comparable mean grain size. There is no consensus on what is a reason for such discrepancy.

As mentioned above the interfacial structures and their evolution in mechanically synthesized nanostructured solids are essentially different from those in conventional coarse-grained polycrystals and nanocrystalline solids synthesized by non-mechanical methods due to high density of severe-deformation-induced non-homogeneities in the interfacial structures as well the presence of high-density ensembles of lattice defects in grain interiors, that strongly interact with the interfaces. In many cases the complicately arranged interfacial structures and their effect on diffusion phenomena in nanostructured metals and alloys can not be unambiguously identified by contemporary experimental techniques [8,9]. This can be studied by theoretical modeling of both the interfacial structures and diffusion processes in materials under study needed to understand their nature and evaluate their potential for practical use.

This review highlights a scientific progress made recently by different groups of scientists united in framework of the project INTAS 99-1216.

Part 2 is devoted to recent developments in fabrication of bulk nanostructured materials by means of severe plastic deformation. Using finite element modeling (FEM) of equal channel angular pressing (ECAP) a distribution of plastic deformation intensity and contact pressure during different friction conditions were obtained. The modeling has shown a high sensibility of plastic deformation uniformity to friction conditions between ingot and die. The results were employed to optimize ECAP process

and to fabricate bulk ingots with uniform nanostructured states in hard-to-deform tungsten and titanium. New results in microstructural characterization of nanostructured materials obtained by high pressure torsion (HPT) is presented. An influence of HPT parameters such as applied pressure, total strain, temperature on the microhardness and microstructural evolution during HPT in samples of pure nickel are discussed.

Part 3 represents some new results on microstructural evolution of ECAP nickel during annealing. Thermal stability is most important issue for ultra-fine grained (UFG) and nanostructured materials. Any successful utilization of nanostructured materials depends upon the subsequent thermal stability of the materials. In practice the microstructures produced by severe plastic deformation are in a metastable condition so that relaxation may occur at significantly lower temperatures than in coarse-grained materials.

Part 4 presents experimental study of GB diffusion in nanocrystalline and nanostructured materials. Higher diffusivity observed in nanostructured nickel processed by SPD methods has been explained by non-equilibrium state of grain boundaries in the materials under study. The consistent model of ordering and diffusion by means of vacancy migration for nanocrystalline and coarse grained materials has been presented. This is a well defined starting point to separate the atomic migration in the crystallites and in the grain boundaries of nanocrystalline materials

Part 5 is devoted to theoretical modeling of grain boundary diffusion in bulk nanostructured materials with special attention paid to the role of non-equilibrium grain boundaries in the diffusion enhancement.

Part 6 has a deal with the influence of GB phase transitions like wetting, prewetting, premelting on the properties of materials. Application of the recently proposed GB phase diagrams is illustrated, particularly for the description of superplasticity in alloys and semi-solid processing of materials. For the first time it was suggested to explain high strain rate superplasticity by the existence of the equilibrium GB liquid-like layer close to the bulk solidus.

Part 7 is related to ordering-reordering kinetics in nanostructured intermetallics processed by mechanical alloying. Short introduction to ball milling is given. The reordering of mechanically disordered Ni₃Al-based alloys was experimentally studied by means of differential scanning calorimetry and magnetization measurements. It is shown that the apparent activation energies of the second stage are very close to the reported values of the activation

energies for ordering and vacancy migration in these alloys. Reordering occurs through the formation and coarsening of ordered domains.

In Conclusion all results are summarized from the viewpoint of advantage of nanostructured materials in comparison to their coarse-grained counterparts. Some examples of application of NS metals and alloys are presented.

2. RECENT DEVELOPMENTS IN FABRICATION OF BULK NANOSTRUCTURED MATERIALS USING SEVERE PLASTIC DEFORMATION

There has been considerable interest over the last decade in processing materials using various techniques of severe plastic deformation in which intense plastic straining is achieved under a high confining pressure [6, 10]. These techniques have the potential of refining the microstructure of metals and alloys to the submicrometer or even the nanometer range. The two most important SPD techniques for producing bulk non-porous samples are equal-channel angular pressing and high-pressure torsion. Fig. 2.1 shows a schematic view of ECA (a) and HPT(b) processing.

Let us review briefly methods of severe plastic deformation suitable for formation of nanostructures. These methods have to meet a number of requirements taken into account while developing them for formation of nanostructures in bulk samples

and billets. These requirements are as follows. First, it is important to obtain ultra fine-grained structures with prevailing high-angle grain boundaries since only in this case a qualitative change in properties of materials may occur. Second, the formation of nanostructures uniform within the whole volume of a sample is necessary for providing stable properties of the processed materials. Third, though samples are exposed to large plastic deformations they should not have any mechanical damage or cracks. Traditional methods such as rolling, drawing or extrusion have not met these requirements. Formation of nanostructures in bulk samples is impossible without application of special mechanical schemes of deformation providing large deformations at relatively low temperatures as well as without determination of optimal regimes of material processing. At present the majority of the obtained results are connected with application of two SPD methods: high pressure torsion [11-24] and equal channel angular pressing [11-15, 24-31]. There are known some investigations on formation of nano- and submicrocrystalline structures in various metals and alloys by means of multiple forging [32-39].

2.1. ECA Pressing

The method of ECA pressing realizing deformation of massive billets via pure shear was developed by Segal and co-workers in the beginning of the eighties [24,27]. Its goal was to introduce intense plastic strain into materials without changing the cross

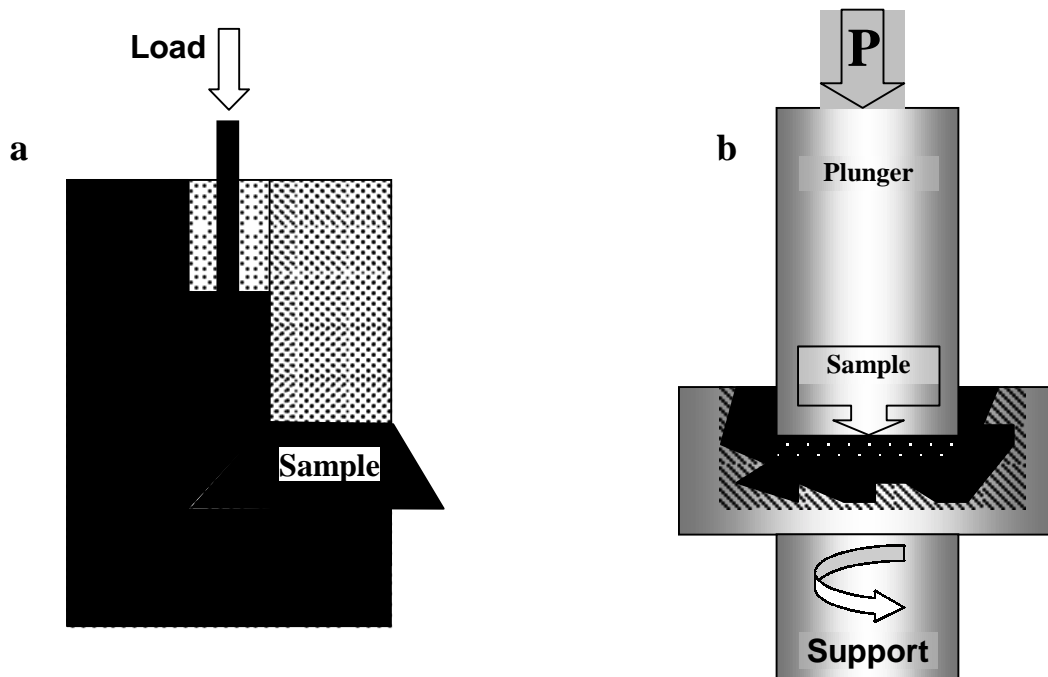


Fig. 2.1. Schematic of ECA (a) and HPT (b) processing.

section area of billets. Due to that, their repeat deformation is possible. In the early 90s the method was further developed and applied as an SPD method for processing of structures with submicron and nanometric grain sizes [11,13,31]. In these experiments the initial billets with a round or square cross section were cut from rods, from 70 to 100 mm in length. The cross section diameter or its diagonal did not exceed 20 mm, as a rule.

During ECA pressing a billet is multiple pressed through a special die using an ECA facility in which the angle of intersection of two channels is usually 90° . If necessary, in the case of a hard-to-deform material, ECA pressing is conducted at elevated temperatures.

A general relationship to calculate the strain value of the billet during ECA pressing for N passes has the following form [25]:

$$e_N = N \times \left\{ \frac{2 \cot(\phi / 2 + \Psi / 2) + \Psi \operatorname{cosec}(\phi / 2 + \Psi / 2)}{\sqrt{3}} \right\} \quad (2.1)$$

Here ψ and ϕ are outer and inner angles, respectively. From this relationship it follows that for the angles, $\phi = 90^\circ$, $\Psi = 20^\circ$, each pass corresponds to an additional strain value approximately equal to 1.

During ECA pressing the direction and number of billet passes through the channels are very important for microstructure refinement. In papers [25,28-30] the following routes of billets were considered (Fig. 2.2): orientation of a billet is not changed at each pass (route A); after each pass a billet is rotated around its longitudinal axis through the angle 90° (route B); after each pass a billet is rotated around its longitudinal axis through the angle 180° (route C). The application of all three routes results in an increase in values of yield stress and strength of a processed material which after several passes achieve saturation [26]. In [31] it was shown also that the first three passes at ECA pressing of Cu and Ni samples lead to a growth of a strain load. Further, there is a stable stage of strengthening and the load does not almost change.

Recently, a series of papers described the microstructural evolution occurring during ECAP has been published and it was shown that the mean grain size and microstructure homogeneity were dependent upon the precise pressing procedure such as routines and temperature described in [28,31,40,41] and friction and strained condition of samples during ECA pressing [42]. Below we discuss recent results on optimization of ECA process-

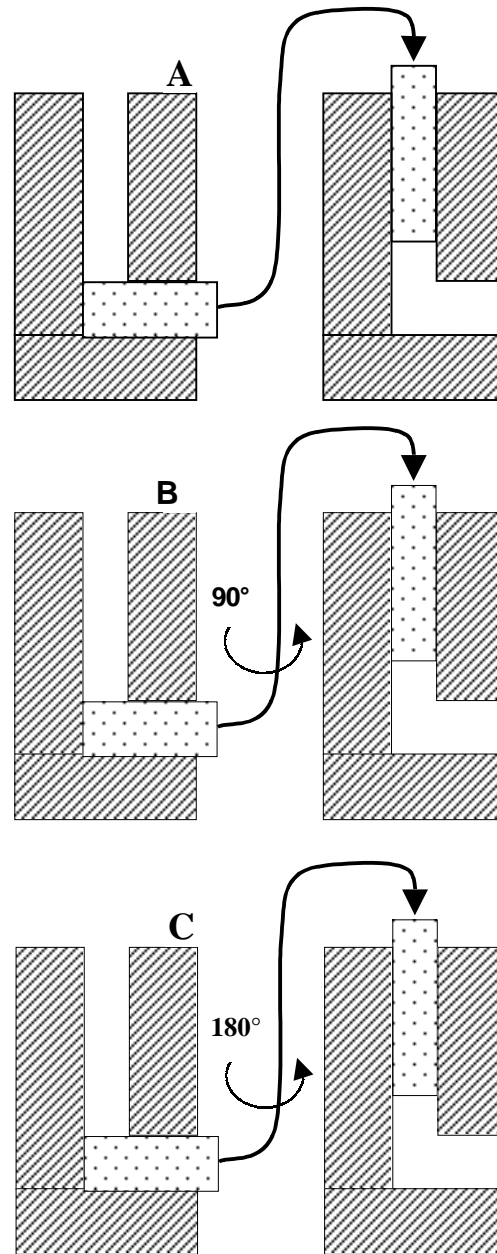


Fig. 2.2. Routes of the ECA pressing [28].

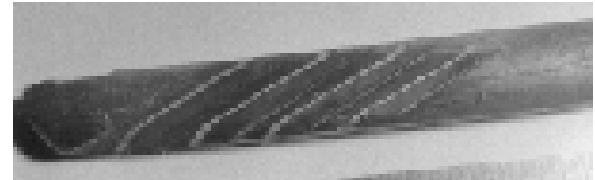
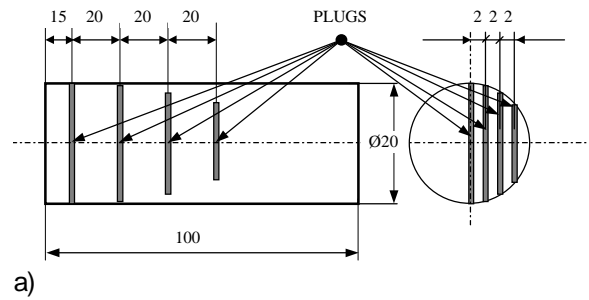
ing in bulk nanostructured metals and alloys including hard-to-deform ones.

Experimental and Finite Element Modeling of ECA processing.

The investigations of the strained condition were conducted on Cu (99.9%) cylindrical ingot with diameter 20 mm and length 100 mm, subjected to one pass pressing at room temperature in ECA die-set with two channels intersecting under 90° (Fig. 2.1). The graphite lubricant was used to decrease friction between ingot and die. At this the coefficient of ingot friction on die walls matches about 0.2. The Al plugs with 2 mm in diameter were embedded into an ingot. The plugs were placed perpendicular to the longitudinal axis in different places

(Fig. 2.3a). As far as SPD by ECA pressing is fulfilled just by simple shear the strained condition were estimated according to the intensity amount of deformation by shear, calculated in respect to the plugs inclination angle φ from their initial state. At this the intensity of deformation by shear was calculated by the formula $\Gamma = \tan \varphi$. The picture of the strained condition in the vertical longitudinal cross section of the ingot coinciding with channels plane indicates the non-uniformity of plastic flow (Fig. 2.3b). The domain of non-uniform deformation about to the lower part of the ingot in cross section and amount to about 10-12% of cross section square. One may suppose that this area can essentially influence the formation of homogenous structure in the ingot during a multiple repeat of ECA pressing. The domain of non-uniform deformation of the upper part of sample cross section is very small and its role may not be considerable during structure development. It was also determined that a strain rate during ECA pressing did not effect essentially the character of non-uniformity in distribution of shear strain. Friction between ingot and die is one of the most important parameters affected the ECA pressing and structure forming character in the wrought ingot. However, it is very difficult to investigate experimentally the influence of this parameter for friction coefficient value $k < 0.2$. In this connection computer simulation was done by finite element technique.

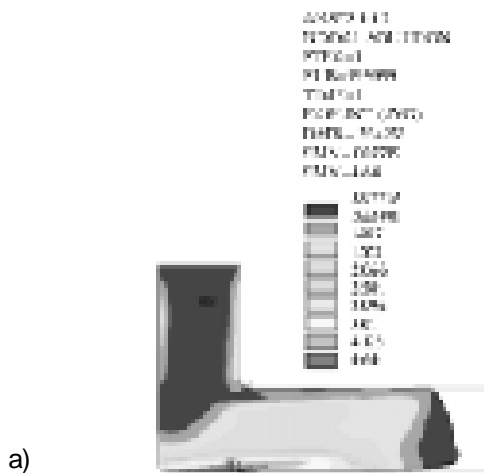
FEM of material plastic flow and strained condition was carried out by the computing code ANSYS 5.5 [43]. The material model with isotropic hardening and diagram of true stress strain behavior for pure Cu was used. The modeling was conducted for channels intersected on the angle of 90° . Friction



a)

Fig. 2.3. The scheme of plugs embedding in the initial ingot (a) and their shape in the cross section of SPD ingot (b).

tion coefficient k was considered as a varying parameter. First, the modeling was conducted with the friction coefficient $k = 0.2$, that conforms to experimental conditions of ECA pressing. The obtained picture indicates that plastic deformation intensity is non-uniform in this case and maximal in the domain adjoining to the outer die angle (Fig. 2.4a). The decrease of friction coefficient k down to 0 resulted in more uniform flow (Fig. 2.4b). Thus, character of the strained condition and uniformity of plastic flow during ECA pressing is very sensible to friction coefficient k . Therefore, one can operate the uniformity of plastic flow of microstructural refinement varying friction conditions.



a)



b)

Fig. 2.4. The distribution of plastic deformations intensity in case of different value of friction coefficient k : $k=0.2$ (a), $k=0$ (b).

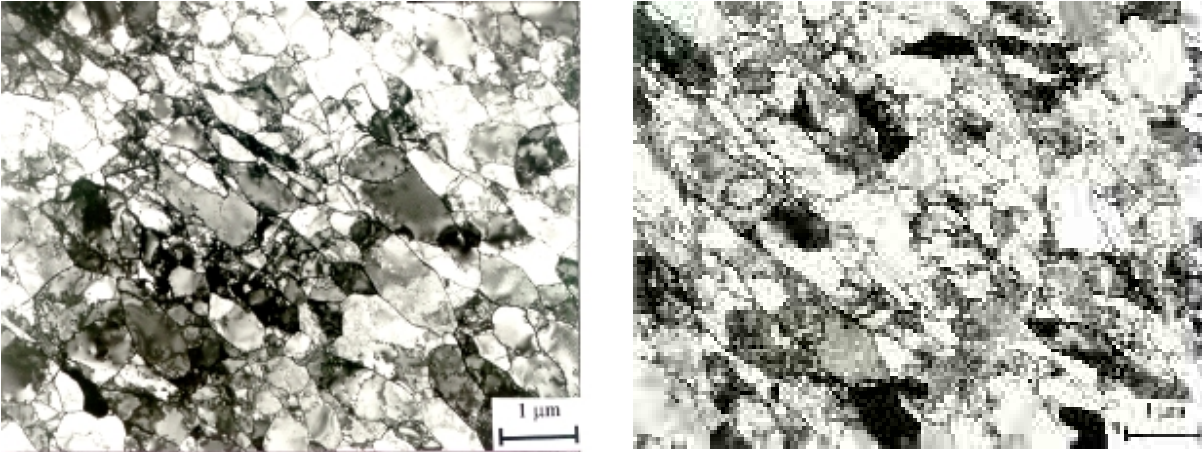


Fig. 2.5. TEM microstructures for ECAP tungsten after 8 passes: normal cross section (a) and longitudinal cross section (b).

Calculation of the contact pressures between ingot and die aimed to choose the material providing workability and safety of forming tool was fulfilled as well. The proportion of applied pressure and contact pressure in the walls of the die-set indicates the necessity to use the die produced of high-strength steels.

Application of Modeling Results. The results of the experimental simulation and FEM of plastic flow and strained condition in SPD ingots enable to choose the most optimal conditions for application of ECA pressing to obtain bulk uniform nanostructured ingots due to fitting of optimal friction conditions. By present time, techniques of obtaining of bulk ingots with uniform ultrafine-grained nanostructures in Cu, Ni and others ductile and relatively easy wrought pure metals and alloys were worked through. Techniques and problems of obtaining such nanostructured states in bulk ingots of hard-to-deform metals including Ti and W could be work out now by modification of the ECA die-set and processing regimes.

As an example, we managed to develop a uniform ultrafine-grained structure with a mean grain size less than 1 μm (Fig. 2.5) by ECA pressing of low ductile and hard-to-deform tungsten in order to enhance strength and plasticity in comparison with the initial state.

By FEM of ECA pressing a distribution of plastic deformation intensity and contact pressure during different friction conditions were obtained. There is a high sensibility of plastic deformation uniformity to friction conditions between ingot and die. The approaches of enhancement of ECA pressing uniformity due to optimization of friction conditions based on the obtained results of experimental and

FEM have allowed to fabricate bulk ingots with uniform nanostructured states in hard-to-deform tungsten and titanium.

2.2. High Pressure Torsion

Devices, where high pressure torsion (HPT) was conducted, were first used in [44,45]. Their design is a further development of the Bridgeman anvil type device [46]. In the first work these devices were used for investigation of phase transformations during heavy deformation [44] as well as evolution of structure and changes in temperature of recrystallization after large plastic deformations [17,18]. Successful formation of homogeneous nanostructures with high-angle grain boundaries via severe torsion straining [6,12,40] was a very important step allowing one to consider this procedure as a new method for processing of nanostructured materials.

The samples fabricated by severe torsion straining are usually of a disk shape, from 10 to 20 mm in diameter and 0.2-0.5 mm in thickness. A significant change in the microstructure is observed already after deformation by 1/2 rotation [19], but for formation of the homogeneous nanostructure several rotations are required, as a rule.

Recent investigations also showed that severe torsion straining can be used successfully not only for the refinement of a microstructure but also for the consolidation of powders [21-23,47,48]. It was revealed that during torsion straining at room temperature high pressures equal to several GPa can provide a rather high density close to 100% in the processed disk type nanostructured samples. For fabrication of such samples via severe torsion straining consolidation not only conventional powders but

also powders subjected to ball milling can be used. The HPT consolidation of nanostructured Ni powder prepared by ball milling [47] can be given as an example. The conducted investigations showed that the density of the fabricated powders is close to 95% of the theoretical density of the bulk coarse-grained Ni. TEM examinations showed the absence of porosity. The mean grain size is very small, it is equal to 17 nm, and, consequently, a large volume fraction of grain boundaries is present. Since grain boundaries have a reduced atomic density the authors assume that the given samples demonstrate a decrease in the theoretical density in the materials with a very small grain size and strong distortions of a crystal lattice. It is also very interesting that a value of microhardness of the Ni samples fabricated by HPT consolidation is about 8.6 GPa. The given value is the highest value of microhardness mentioned in literature for the nanocrystalline Ni.

Speaking about HPT processing we can note that only recently detailed investigations have been conducted to evaluate the parameters influencing HPT (e.g., applied pressure, total strain, temperature). In earlier reports, it was found for several metals and alloys that a pressure of ~5 GPa and more than five rotations of the sample in torsion were generally sufficient to produce a reasonably homogeneous microstructure with a mean grain size close to ~100 nm throughout the sample [49-52]. Below new results [51] on the microhardness and microstructural evolution during HPT in samples of pure nickel are discussed in details.

Microstructure Evolution in Nickel during High-pressure Torsion. High purity nickel (99.99%) was selected as the material for investigation. This section reports the results obtained on Ni samples subjected to annealing prior to high-pressure torsion, where all samples were annealed for 6 hours at 700 °C to give an initial grain size of ~100 μm and a microhardness of ~1.4 GPa. During the early stages of this study it was found that the final microstructure produced by HPT is independent of the initial grain size within the range of ~1 – 100 μm . Electro-discharged samples in disk shape, with diameters of ~10 mm and thickness of ~0.3 mm, were subjected to HPT straining under different applied pressures and with different numbers of whole revolutions at room temperature. Fig. 2.1b schematically depicts the HPT method. A disk is placed between anvils and then compressed and deformed under an applied pressure (P) of several GPa at room temperature. The lower holder rotates and surface friction forces deform the disk by shear so that deformation proceeds under a quasihydrostatic pressure. Further details

of HPT processing are given elsewhere [10, 40]. To evaluate the influence of the applied pressure, samples were produced with 5 whole turns at separate pressures of 1, 3, 6 and 9 GPa. The influence of the accumulated strain was evaluated by using a pressure of 6 GPa and totals of $\frac{1}{2}$, 1, 3, 5 and 7 turns. Precise microhardness measurements were taken on both sides of the samples along two perpendicular diameters and with incremental steps of ~1.25 mm between each measurement. At every point, the average microhardness was determined from four separate measurements. The total number of measurements was not less one hundred for each sample. For the samples deformed at pressures of 1 and 6 GPa, foils were prepared from both the centers and the perimeters of the disks for examination by TEM.

Experimental results. The processing of nickel by HPT leads to an increase in the microhardness, Hv , due to significant microstructural refinement that is strongly influenced by the processing parameters. Fig. 2.6 shows (a) the influence of the applied pressure on the microhardness profile across the disk and (b) the average values of Hv measured in the central region and close to the edge. In Fig. 2.6a, these microhardness values are higher than for the unprocessed nickel (~1.4 GPa) but at the lower applied pressure of 1 GPa there is a non-uniform distribution of microhardness across the sample diameter with significantly lower values in the center. An increase of pressure to 9 GPa leads to an increase in the values of Hv , especially in the center of the disk. Thus, there is an increased uniformity in Hv across the disk with increasing applied pressure such that the variation in Hv is not more than ~7% for the sample subjected to a pressure of 9 GPa. Figure 2.6b reveals the dependence on applied pressure of the average microhardness taken from the center and edge of the disks, with the microhardness at the edge appearing to exhibit a plateau. By contrast, the central region has a relatively low level of microhardness up to a pressure of 6 GPa but thereafter the microhardness increases and is close to the value measured at the edge. The apparent slight decrease in Hv for applied pressures from 1 to 3 GPa is within experimental error and is probably not significant. A TEM examination was performed for two different applied pressures of 1 and 6 GPa and with foils cut from the center and the edge of the samples. Figures 2.7a and b show two bright field images of the microstructures at the center and edge regions of the sample after HPT at 1 GPa: the corresponding selected area electron diffraction (SAED) patterns are

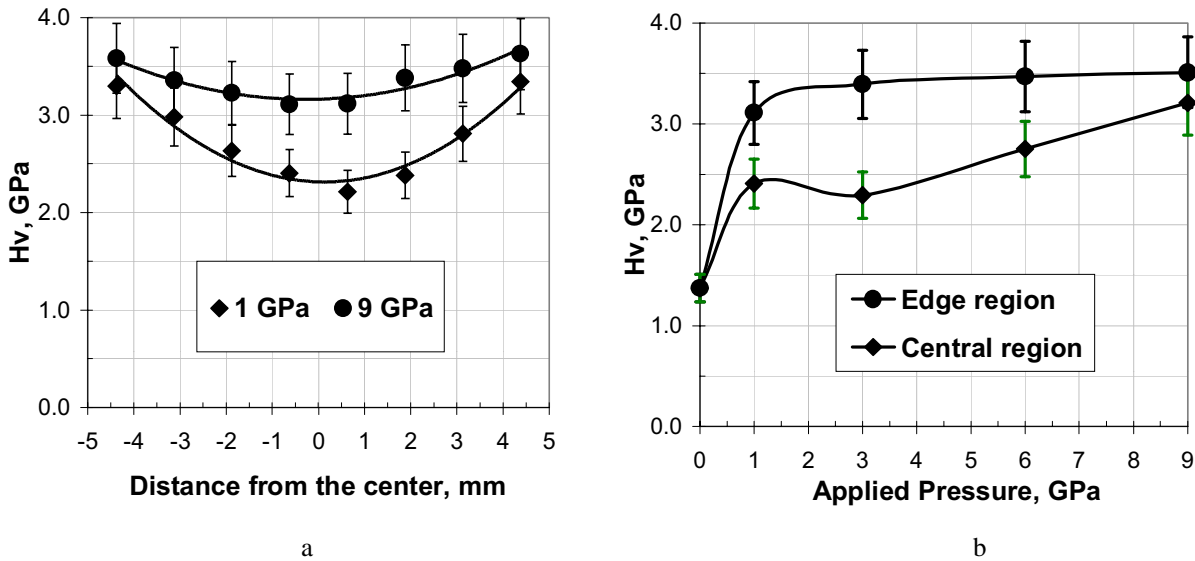


Fig. 2.6. Microhardness profile of HPT processed nickel at two different applied pressures (a); average microhardness for the central and edge regions of HPT nickel as a function of applied pressure (b). Samples were subjected to HPT pressing at room temperature through 5 whole turns.

shown as inserts. It can be seen that the microstructures have important differences. Microstructural refinement is higher near the edge of the disk and the mean grain size in this region was measured as $\sim 0.17 \mu\text{m}$. The SAED pattern in Fig. 2.7 b contains many spots situated around circles indicating the presence of boundaries having high

misorientation angles. By contrast, the SAED pattern in the center of the disk in Fig. 2.7 a consists of separate spots showing the presence of low angle subboundaries. The measured average size of the subgrains in Fig. 2.7 a is almost two times larger than the grain size in Fig. 2.7 b. In both cases, the azimuthal spreading of spots in the SAED patterns

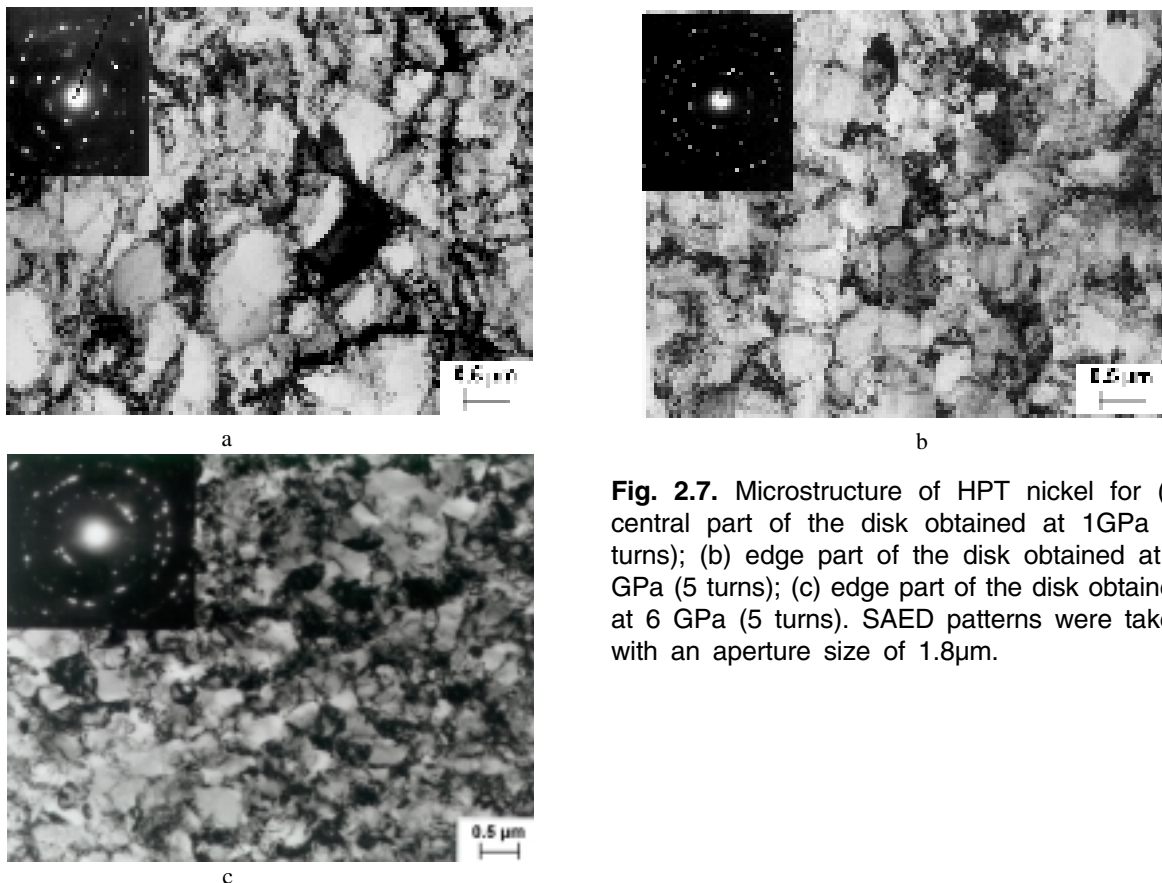


Fig. 2.7. Microstructure of HPT nickel for (a) central part of the disk obtained at 1 GPa (5 turns); (b) edge part of the disk obtained at 1 GPa (5 turns); (c) edge part of the disk obtained at 6 GPa (5 turns). SAED patterns were taken with an aperture size of $1.8 \mu\text{m}$.

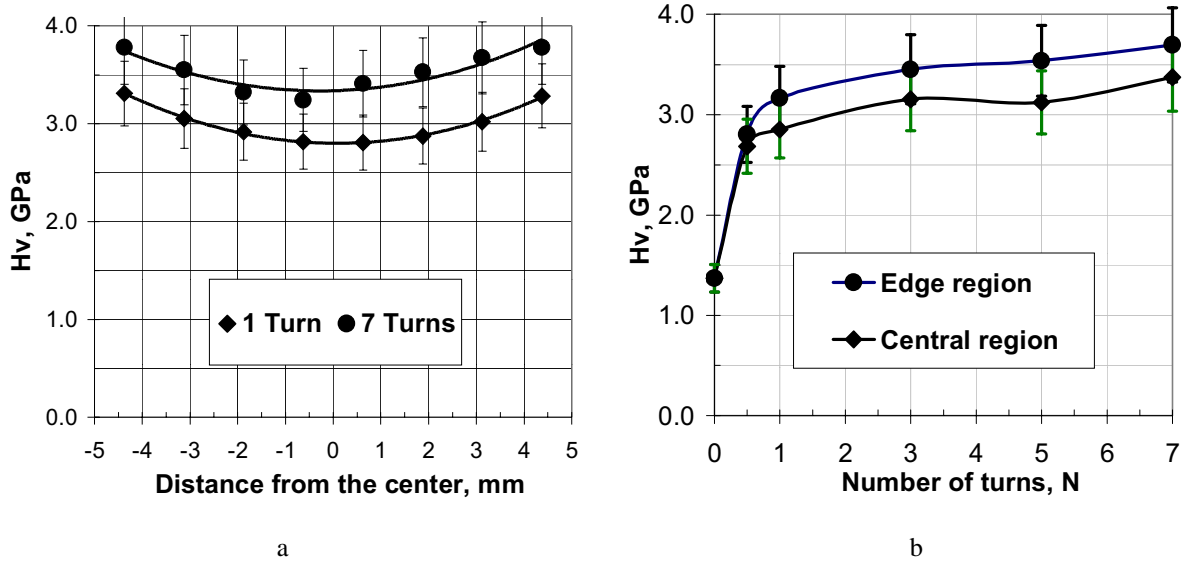


Fig. 2.8. Microhardness profile of HPT processed nickel at two different numbers of whole turns (a); average microhardness for the central and edge regions of HPT nickel as a function of number of turns (b). Samples were subjected to HPT pressing at room temperature with a pressure of 6 GPa.

indicates the presence of high internal stresses. The situation was different for the sample subjected to HPT at 6 GPa, as shown at the edge of the sample in Fig. 2.7 c. The microstructures for this condition were reasonably similar at both the center and the edge, and the SAED patterns consisted of rings with many diffracted beams so that there were many small grains with multiple orientations within the selected fields of view. The average grain size was measured as $\sim 0.17 \mu\text{m}$ for both areas. Detailed high-resolution electron microscopy (HREM) and TEM were reported recently for this condition [53] and it was shown that the grain boundaries in HPT-processed Ni generally have high misorientation angles and they exhibit *zigzag* configurations and irregular facets and steps that are indicative of high-energy non-equilibrium structures. Figure 2.8 shows the influence of the number of rotations on Hv in samples processed at an applied pressure of 6 GPa. As in the profile shown in Fig. 2.8 a, there is a difference in the microhardness values measured at the center and the edge of the disk. However, this difference becomes relatively less after larger numbers of turns because of the overall increase in the microhardness level. An increase in the number of rotations leads to an increase in Hv at both the center and the edge of the sample, as shown in Fig. 2.8 b.

It is known for torsion deformation that the shear strain, γ , at a radius R is given by

$$\gamma = \log\left(\frac{2\pi RN}{L}\right), \quad (2.2)$$

where N is the number of turns and L is the thickness of the sample. According to this relationship, the true logarithmic strain is larger than 6 for five rotations of a sample having a thickness of 0.3 mm and at the radius of 5 mm. Such very large cold deformation produces a very significant refinement of the microstructure and the formation of an array of ultra-fine grains leading to increased microhardness [40]. At the same time, it follows from Eqn. (2.2) that significant grain refinement cannot occur in the center of the samples because the straining is then very much reduced. In practice, however, this is true only for small numbers of turns and relatively low applied pressures and the present experiments demonstrate that an increase in the straining leads to an increase in the homogeneity of the microstructure (Fig. 2.8). It is concluded that samples processed with more than ~ 5 turns are capable of producing reasonably homogeneous ultrafine-grained microstructures. This must be associated with the accumulation of dislocations within the disks but the mechanism of microstructural homogeneity requires further investigation.

An additional important processing parameter is the applied pressure. The role of pressure is not apparent from Eqn. (2.2) but the experimental results show that higher pressures facilitate the formation of ultrafine-grained microstructures. A simi-

lar conclusion was reached recently from HPT studies of iron [20] and titanium [22]. It is well known that the applied pressure can reduce the rate of diffusion and consequently delay the recovery kinetics [54] and this may explain the smaller grain sizes generally achieved by HPT at higher pressures.

3. THERMAL STABILITY AND MICROSTRUCTURE EVOLUTION IN SPD MATERIALS DURING ANNEALING

Any successful utilization of nanostructured materials will depend upon the subsequent thermal stability of the ultrafine-grained structures and in practice the microstructures produced by severe plastic deformation are in a metastable condition so that relaxation may occur at significantly lower temperatures than in coarse-grained materials. It's known that the onset of grain growth begins in nanostructured materials at relatively low temperature ($0.4 T_M$). An investigation of low thermostability's origin is very important for understanding processes occurring in NS materials during annealing. The microstructure evolution and grain growth were a main object in recent publications [49,55-63]. TEM investigations and x-ray analysis were carried out in pure metals: nickel [51,58,61], copper [49,50,62], cobalt [61], iron [55] where the temperatures of grain growth onset have been identified and intensive relaxation processes have been noticed. However, the characteristics of grain growth have many particularities and need to be studied more extensively.

There are earlier reports of microstructural evolution and thermostability in copper [49,50] and nickel [51] processed by HPT but there are no detailed studies for materials processed using ECAP. This method is especially attractive because it has the potential of producing relatively large billets that may have use in industrial applications. This part of review presents recent findings [64] of the changes in microhardness and microstructure occurring in pure nickel during annealing after processing by ECAP.

Experimental Material and Procedure. Cylindrical billets, with diameters of 16 mm and lengths of 130 mm, were machined from high purity (99.99%) nickel. The initial grain size was $\sim 30 \mu\text{m}$. The billets were subjected to ECA pressing at room temperature using the equipment shown schematically in Fig. 3.1. All samples were pressed repetitively through a total of 8 passes under an imposed pressure of 800 MPa. Each sample was reversed from end to end and rotated by 90° about the longitudinal

axis between each pass. The total logarithmic strain accumulated in the samples was approximately $e = 8$. Further details on processing by ECAP are given elsewhere [28,30,40]. For annealing and microhardness testing, small disks were electro-discharged from the central part of the as-pressed cylinders. The annealing treatment was conducted in air for 3.6 ks at temperatures from 373 to 773K and also at 523K for periods of 3.6, 21.6 and 43.2 ks. After annealing, the surfaces of all samples were ground to remove any oxide film and they were then mechanically and electrochemically polished for microhardness testing. The microhardness, H_v , was measured using a Vickers diamond pyramidal indenter under a load of 100 g. Samples were examined by transmission electron microscopy (TEM) using a JEM-100B electron microscope. For the samples annealed at the highest temperatures of 573 – 773K, the microstructures were examined using both TEM and optical microscopy.

Experimental Results and Discussion. After processing by ECAP, the microhardness of Ni was measured as $H_v = 2.6 \text{ GPa}$ and the mean grain size was $\sim 0.35 \mu\text{m}$. By comparison, the initial microhardness of an unpressed sample annealed for 3600 s at 773K was $H_{v0} \approx 1.0 \text{ GPa}$. Samples were annealed for 3600 seconds at different temperatures and the measured values of the microhardness and the mean grain size, d , are summarised in Table 3.1: grain sizes were measured by TEM up to annealing temperatures of 523K and by optical microscopy at the higher temperatures. For convenience, the experimental data are plotted in Fig. 3.1. The microhardness tests reveal a slight decrease in H_v for annealing temperatures up to 473K,

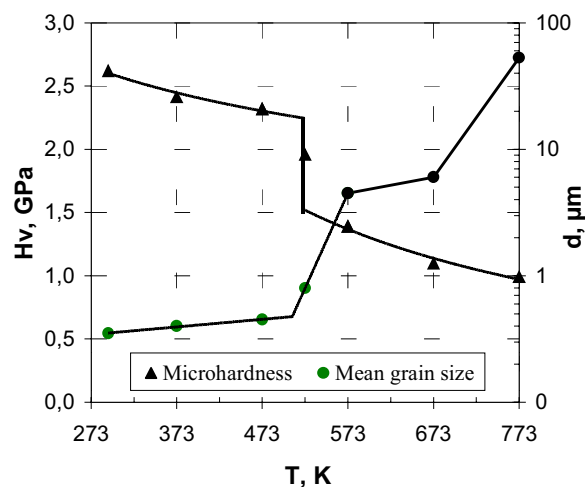


Fig. 3.1. Microhardness and mean grain size vs. annealing temperature for an annealing time of 3600 s.

Table 3.1. Microhardness and mean grain size as a function of annealing temperature.

| Temperature, K | 293 | 373 | 473 | 523 | 573 | 673 | 773 |
|--------------------------------|------|------|------|------|-----|-----|-----|
| Microhardness, GPa | 2.6 | 2.4 | 2.3 | 2.0 | 1.4 | 1.1 | 1.0 |
| Mean grain size, μm | 0.35 | 0.40 | 0.45 | 0.80 | 4.5 | 6.0 | 53 |

a sharp drop at temperatures from 473K to 573K and then a slow decrease to a value of ~ 1.0 GPa appropriate to the well-annealed condition.

All annealed samples were examined by TEM to evaluate the microstructural characteristics. Typi-

cal microstructures are shown in Fig. 3.2 corresponding to (a) the as-preserved condition without subsequent annealing and after annealing for 3600 seconds at temperatures of (b) 373, (c) 473, (d) 523, (e) 573 and (f) 673K, respectively. In Fig. 3.2(a), the

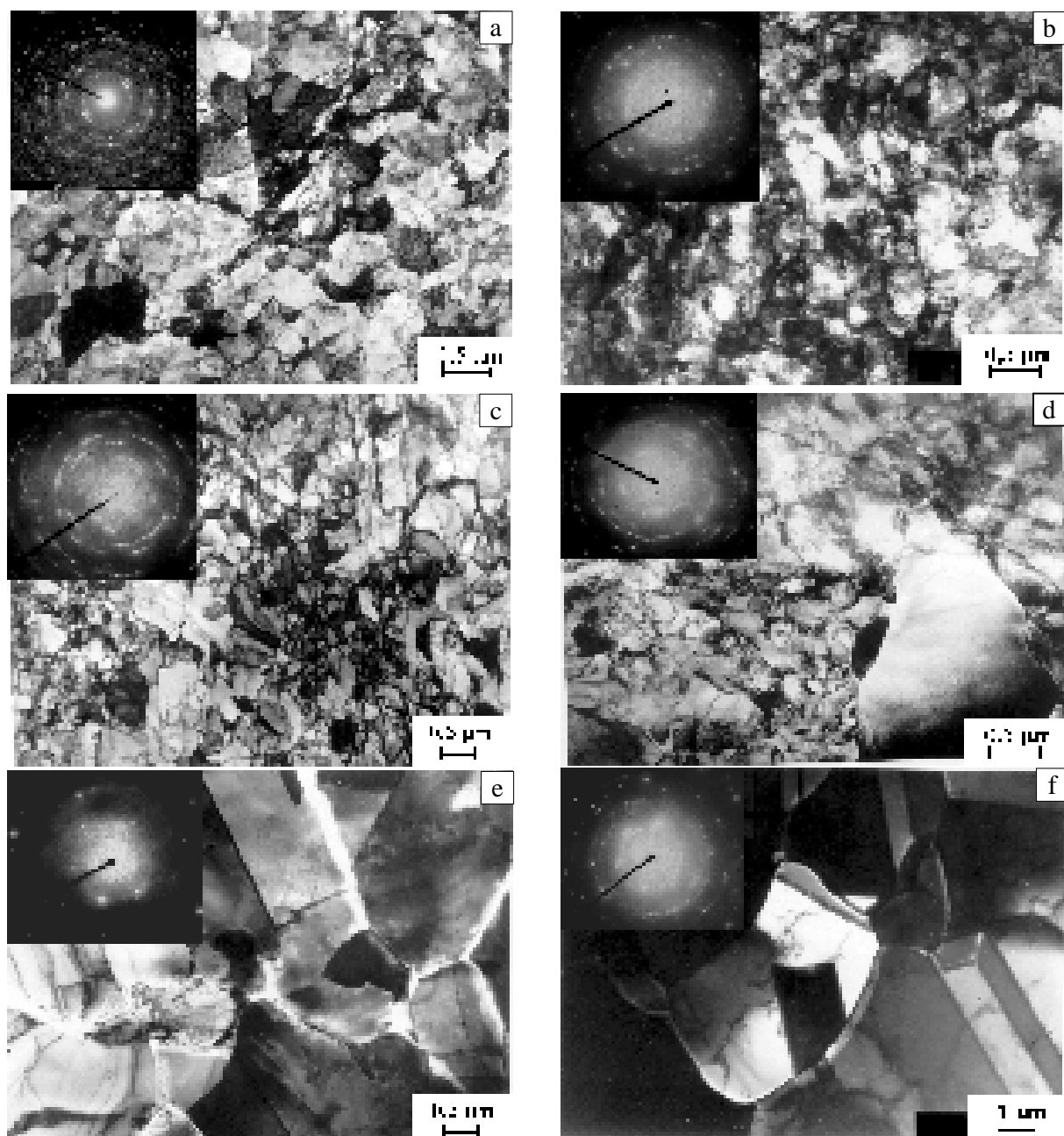


Fig. 3.2. TEM microstructure of ECAP nickel annealed at different temperatures for 3.6 ks: a – as received; b – 373K; c – 473K; d – 523K; e – 573K; f – 673K.

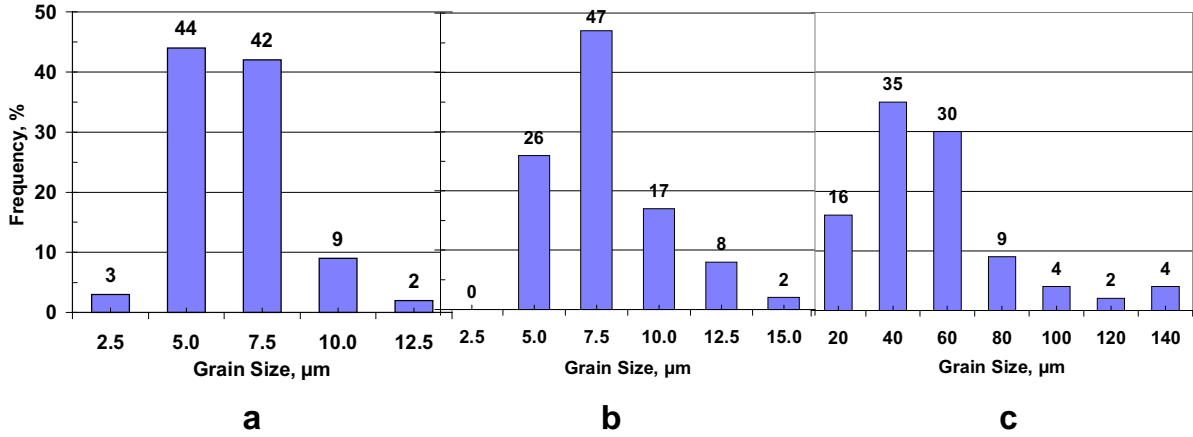


Fig. 3.3. Grain size distributions in nickel annealed for 3600 s at temperatures of (a) 573K, (b) 673K and (c) 773K.

as-pressed microstructure is typical of pure metals after severe plastic deformation: there is an array of essentially equiaxed grains, the boundaries have irregular configurations and the azimuthal spreading of the spots in the selected area electron diffraction pattern suggests the presence of high internal stresses. Annealing at temperatures of 373 and 473K has a minor effect on the grain size but there is noticeable grain growth at the relatively low temperature of 573K in Fig. 3.2 e corresponding to $\sim 0.33T_M$, where T_M is the absolute melting temperature of the material. There is also evidence at this temperature for some twinning in the grain interiors. At the higher annealing temperature of 673K in Fig. 3.2 f, there are few intragranular dislocations, the boundaries have equilibrium configurations and the microstructure is typical of well-annealed coarse-grained materials.

Typical grain size distributions are shown in Fig. 3.3 for the samples annealed at the three highest temperatures. It is apparent that the grain size distributions in Figs. 3.3 a and b are close to log-normal corresponding to normal grain growth but the grain size distribution in Fig. 3.3 (c) is bimodal with a small secondary peak appearing at large grain sizes of ~ 130 – 140 μm . This suggests the onset of abnormal grain growth at 773K. Fig. 3.1 demonstrates that the grain growth kinetics and the microhardness measurements are consistent: there is a gradual increase in the grain size in the temperature range of 373–473K and a sharp increase in d , by a factor of 10 times, from ~ 0.45 μm at 473K to ~ 4.5 μm at 573K. Fig. 3.3 shows the influence of the annealing time on microhardness and grain growth kinetics at a temperature of 523K. The time dependence of the microhardness and the

mean grain size therefore demonstrate similar behaviour. It is well established that grain growth kinetics can be described by the relationship [65]:

$$d^2 - d_0^2 = kt^n, \quad (3.1)$$

where d_0 is the initial grain size, k is a constant depending on the driving force for grain growth and the mobility of the grain boundaries and n is a constant typically lying in the range from 0.5 to 1.

Grain growth kinetics with $n = 1$ correspond to the parabolic law and normal grain growth. By fitting the experimental points to Eq. (3.1) by means of a least squares method, the value of the constant k was determined as $0.6165 \mu\text{m}^2 \cdot \text{h}^{-1}$ or $170 \text{nm}^2 \cdot \text{s}^{-1}$. The solid line in Fig. 3.4 is plotted using Eq. (3.1) with $n = 1$ for the parabolic law. Assuming parabolic kinetics are fulfilled for all annealing temperatures, it is possible to calculate the activation energy, Q , and the pre-exponential factor, k_0 , for the grain growth process using the expression $k = k_0 \exp(-Q/RT)$, where Q is the activation energy for grain growth, R is the gas constant and T is the absolute temperature. From a best fit to the experimental data, it was found that $k_0 = 3.9 \cdot 10^{-6} \text{m}^2 \cdot \text{s}^{-1}$ and $Q = 103 \text{kJ} \cdot \text{mol}^{-1}$. This value for Q is very close to the values of the activation energies reported for grain boundary diffusion in nickel ($115 \text{kJ} \cdot \text{mol}^{-1}$ [66], $131 \text{kJ} \cdot \text{mol}^{-1}$ [67] and $108.8 \text{kJ} \cdot \text{mol}^{-1}$ [68]). In addition, the value of the kinetic constant may be evaluated directly by making use of the relationship [65]:

$$k_0 = \frac{4\gamma\Omega}{\delta^2} \cdot \frac{\delta D_{ob}}{kT}, \quad (3.2)$$

where γ is the grain boundary surface energy ($\sim 0.7 \text{J} \cdot \text{m}^{-2}$), Ω is the atomic volume ($1.1 \cdot 10^{-29} \text{m}^3$), δ is

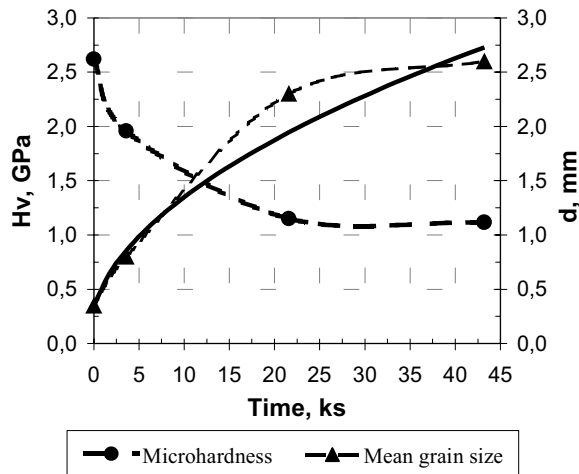


Fig. 3.4. Microhardness and mean grain size vs. annealing time at 523K: the solid line shows the parabolic law for grain growth.

the grain boundary width ($\sim 0.7 \cdot 10^{-9}$ m), $\delta \cdot D_{gb}$ is the pre-exponential factor for grain boundary diffusion multiplied by the grain boundary width ($\sim 3.5 \cdot 10^{-15}$ $\text{m}^3 \cdot \text{s}^{-1}$), k is Boltzmann's constant and T is the absolute temperature. Taking a value of $T = 500\text{K}$, it follows from Eq. (3.2) that the value calculated for k_0 is given by $(k_0)_{\text{cal}} \approx 4.6 \cdot 10^{-5}$ $\text{m}^2 \cdot \text{s}^{-1}$. This value is consistent with the experimental value to within approximately one order of magnitude, thereby confirming the validity of the present approach.

Thus, the calculation demonstrates that grain growth kinetics in ultrafine-grained nickel processed by ECAP is controlled by grain boundary diffusion and possibly by other short-circuit diffusion paths that may exist in nanostructured materials. This result is consistent also with the recent conclusion that grain boundary diffusion dominates grain growth in nanostructured nickel prepared by electrodeposition [66]. This investigation shows that the relaxation processes in ultrafine-grained nickel, processed by equal channel angular pressing, undergo 3 distinct stages. The first stage corresponds to the temperature range of 373-473K and represents a relaxation of the internal stresses arising from the ECAP process. The second stage takes place within the temperature range of 473-573K where there is a sharp drop in the microhardness and an abrupt increase in the grain size due probably to subgrain coalescence and dislocation annihilation. The third stage relates to normal grain growth at temperatures above $\sim 573\text{K}$ ($\sim 0.33T_M$) where the rate-controlling process is grain boundary diffusion. This latter temperature is relatively low for normal grain growth but it is consistent with the decrease in thermal stability observed in ultrafine-grained metals

processed by severe plastic deformation. The results demonstrate a good correlation between the microhardness measurements and microstructural observations following ECAP and annealing.

4. GRAIN BOUNDARY DIFFUSION IN NANOSTRUCTURED MATERIALS

4.1. The characteristics of copper grain boundary diffusion in nanocrystalline and nanostructured materials

Diffusion in nanocrystalline materials is very important for their properties. Therefore, it is studied very actively [69-78]. The keen interest in this theme is stipulated, among other reasons by the fact that diffusion exerts primary control over the kinetics of recovery and recrystallization processes occurring in nanocrystalline materials at significantly lower temperatures relative to the coarse-grained materials. It has also been proven experimentally that nanocrystalline systems have "anomalously" high diffusivity, which is an additional reason for this high interest [69,70,73]. It has been found that the high diffusivity results not only from the high volume fraction of the "GB phase" in such materials but also mostly from residual porosity, impurity segregation and other factors related to a processing routine of nanocrystalline materials [76-78].

In particular, porous nanocrystalline metals produced by the methods of gas condensation and electrolytic deposition are found to reveal low-temperature anomalies of GB diffusion. Their diffusivities are several orders of magnitude higher and the activation energies of self-diffusion and of substitution impurity diffusion are about two orders lower in comparison to the coarse-grained materials [69,72,73]. In case of interstitial impurities, the diffusion processes depend essentially on the kind of impurity [74,78]. The "anomalies" of GB diffusion are not observed in materials after recovery and recrystallization [75].

Non-porous nanocrystalline materials (in particular those obtained by explosive pressing) are found to reveal no "anomalous" diffusion behavior [75-78], which suggests that intrinsic free surfaces play a significant role in the evolution of diffusion processes in nanocrystalline materials [72].

The existing physical models take into account the peculiar properties of GBs in nanocrystalline materials. Thus the model of glue-like grain boundary state, which was developed on the base of computer simulation results, takes into account the

correlation effects, which are exhibited by ultrafine-grained materials and which are associated, in particular, with the absence of relaxation effects due to the generation of dislocations induced in such materials [79]. One of the basic assumptions of the cluster model based on HREM examination consists of the important role played by the boundaries of ensembles of adjacent grains – “clusters”, on which grain-boundary pores occur and the main portion of excess (free) volume of nanocrystals is concentrated [73].

Investigators to date focus their attention on the role of triple junctions. The density of these linear defects in nanocrystalline materials is considerably higher relative to their coarse-grained counterparts. The occurrence in the bulk of a continuous network of triple junctions and concentration of most pore volume in the latter assists a creation of short diffusion paths in nanocrystalline materials [74].

The available data on diffusion in nanocrystalline materials and the results of other physical investigations of these materials are summarized in [69,72,75,78].

R. Würschum, H.-E. Schaefer and others [69,72,75,78-81] were the first to investigate diffusion in nanostructured materials produced by severe plastic deformation, in particular ^{59}Fe diffusion in Pd. While the authors of the given work performed diffusion experiments at the temperature above 410K they failed to reveal any significant increase in the grain boundary diffusivities of the investigated materials. However, the experimentally measured diffusivities observed for nanostructured materials at lower temperatures (371K and 471K) were by about two orders of magnitude higher relative to the respective coarse-grain samples [75]. As in the case of nanocrystalline metals, the activation energy of grain-boundary diffusion in nano-Pd turned out to be significantly lower (by 1.5 times) as compared to coarse-grained Pd. It should be noted that in the experimental conditions of diffusion annealing [75] GB migration was found to occur, which has to be taken into account in choosing a particular model for evaluating materials diffusivity. Moreover, during grain boundary migration a change in the grain boundary state may occur and it can influence the diffusivity value. Thus it appears that material's diffusion parameters may be significantly affected by the recovery of the grain boundary structure in nanostructured-Pd that occurs during diffusion annealing at elevated temperatures [75]. Recently the investigation of self-diffusion in nanostructured-Fe was performed; the results obtained indicate that no “anomalous” increase in the grain boundary

diffusivity takes place in the material investigated [76,77].

A comparative study of the diffusion parameters of nanostructured and coarse-grain metals was conducted for copper diffusion in nickel [82-84]. The concentration of Cu in Ni was measured at various depths by the method of secondary ion-mass spectroscopy using the technique described elsewhere [83]. The activation energy of the grain boundary diffusion of Cu in coarse-grained Ni, Q_b , was determined in the temperature interval of 773 to 873K; the value obtained was 124.7 kJ/mol (Fig. 4.1). Assuming that in the entire temperature interval considered, the Arrhenius dependence parameters for the coefficients of grain boundary diffusion are constant, the respective values were calculated for coarse-grained Ni at lower temperature [84].

According to TEM data reported in [83], no GB migration in nanostructured Ni is likely to occur in the temperature interval of 392–448K and the volume diffusion may be virtually suspended. Therefore, the values of the GB diffusivity were calculated basing on the assumption that the experimental conditions of diffusion annealing are close to regime C. In the C regime the pure GB grain boundary diffusion proper takes place without leakage of the diffusant into the bulk [85]. It has been found that the GB diffusion coefficients, D_n , obtained for Cu diffusion in nanostructured Ni are by 4 to 5 orders of magnitude higher relative to coarse-grain Ni (Fig. 4.1) [84].

From the temperature dependence of D_n of Cu in nanostructured Ni we obtained the activation energy of grain boundary diffusion $Q_b^n = 43.5$ kJ/mol [84]. The latter value is by a factor of two lower than the respective value for coarse-grained nickel samples (Fig. 4.1). Unlike the diffusion in nanocrystalline metals containing pores at GBs [69-78], the activation energy of grain boundary diffusion in nanostructured pore-free nickel is close to that of surface diffusion [84]. Moreover, the activation energy value of the grain boundary diffusion of Cu in nanostructured Ni is close to the activation energy of the GB self-diffusion (46 kJ/mol, Fig. 4.1) [73].

As noted above, the GBs in nanostructured metals are characterized by a highly nonequilibrium (high-energy) state, while the GB state in nanocrystalline and coarse-grain metals is close to an equilibrium one. Therefore, the values D_n obtained for nanostructured nickel are significantly higher comparing to nanocrystalline Ni [73,84] and coarse-grain counterparts. It suggests that the GB diffusion of impurity atoms in the investigated materials is mainly determined by GB state and less by other

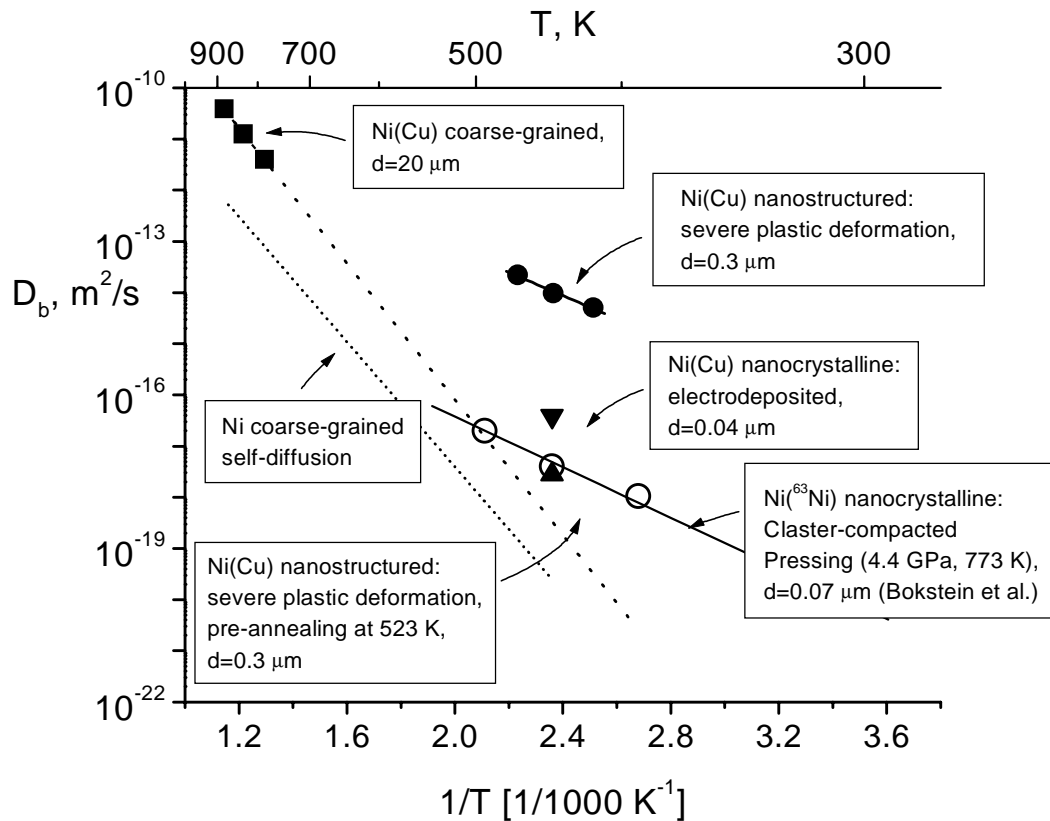


Fig. 4.1. Arrhenius plot for the GB diffusion coefficient (D_b) of copper in nickel possessing different structure: coarse-grained (CG, ■), nanostructured electrodeposited (ED, ▲), nanostructured after severe plastic deformation (SPD) – as-prepared (●) and subjected to pre-annealing at 523K for 1 h (▼). d – grain size of the material; diffusion width d is assumed to be 1 nm.

parameters like mean grain size [84]. If the GBs in nanostructured Ni recover into an equilibrium state, D_n is expected to decrease. Indeed, the maximum value of D_n obtained for nanostructured nickel subjected to preliminary annealing for 1 h at 523K followed by diffusion annealing for 50 h at 428K was by four orders of magnitude lower relative to the same material in as-received state (Fig. 4.1). Thus an increase in the grain diffusion in nickel samples investigated is mainly associated with the nonequilibrium state of the material. This is demonstrated by one order of magnitude reduction in D_n observed in nickel samples kept at 423K for three years [84].

Thus, the GB diffusivities are found to increase in both nanostructured metals produced by severe plastic deformation and porous nanocrystalline metals. Direct diffusion experiments have shown that higher rates of mass transfer in the above metals are related to a nonequilibrium high-energy state of the materials' interfaces rather than with their grain size. The above anomalies and the predominant role of GB state are also observed for the same class of materials having no GB porosity and with grain size

in the range of 0.3–0.5 mm (the existence of significant correlation effects being highly unlikely). Therefore, the currently known models of diffusion mechanisms along grain boundaries do not apply when the above peculiarities of diffusion have to be accounted for, especially in the case of nanostructured materials produced by severe plastic deformation.

It is an established fact that metals and alloys subjected to preliminary deformation have somewhat higher diffusivities along GBs (generally by an order of magnitude) relative to their counterparts subjected to recrystallization [86]. The method of severe plastic deformation allows one to attain high levels of deformation and high density of defects in both grain volume and on the grain boundaries. At the same time, the observed increase in grain boundary diffusivity by at least four orders of magnitude [84] has to be verified experimentally with the aid of various techniques.

4.2. Grain boundary diffusion – ordering coupling in nanocrystalline materials

The transport of atoms by diffusion determines, e.g., the thermal stability, sintering properties, creep or ion conductivity in oxides. The high number of interfaces in nanocrystalline materials can change the macroscopic diffusion behavior considerably with respect to coarse grained materials. For example, the self-diffusivity in grain boundaries of metals is normally strongly enhanced due to the relative loose packing of atoms in these interfaces. Therefore, the activation enthalpy for jumps of atoms is lower than in the perfectly ordered crystal and vacancies like voids, which act as diffusion vehicles, can be formed easily.

However, for a full understanding of the diffusional properties, one has to take into account not only the diffusion in the interfaces, but also in the crystallites. The volume diffusion into the crystallites becomes more pronounced at longer diffusion times or higher temperatures, which are often application relevant. E.g., the oxygen diffusion in nanocrystalline ZrO_2 [78, 87], which could be used as a solid state electrolyte for fuel cells, is determined by both diffusion processes.

Fig. 4.2 gives an overview on the experimental work done or in progress to obtain an atomistic understanding of the diffusion processes in nanocrystalline materials. Structural studies (X-ray dif-

fraction and transmission electron microscopy (TEM)) provide the necessary input for conclusions on the correlation between diffusion and structure. Positron annihilation spectroscopy is a technique specific and sensitive on vacancies or vacancy clusters and was successfully employed to investigate voids at grain boundaries [88]. Further insight comes from theoretical studies to model equilibrium (see, for example, Chapter 6) and non-equilibrium (Chapter 5) grain boundaries.

High-resolution TEM studies on nanocrystalline materials prepared by cluster condensation and compaction concur with a randomly distributed crystallite orientations and mostly high-angle grain boundaries (see Fig. 4.3 [78]). In many nanocrystalline pure face-centered cubic (fcc) metals these boundaries exhibit diffusivities similar to high-angle grain boundaries in coarse grained materials [89]. In nanocrystalline Fe [76] and Ni (Chapter 4.1) diffusivities were found which are higher than for high-angle grain boundaries in the corresponding coarse grained materials. The structure of the grain boundaries of these nanocrystalline materials relax with time towards the equilibrium state of coarse grained materials as indicated by the decreasing diffusivities.

Diffusion studies on composite materials or alloys become more and more important because of a more pronounced stability against grain growth. Nevertheless, studies on pure systems remain important as reference for the diffusion in composite materials or alloys. Fig. 4.4 shows as an example

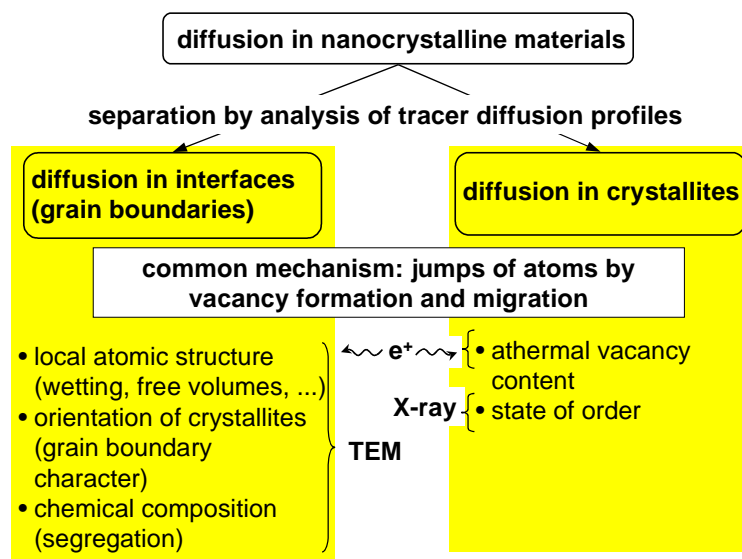


Fig. 4.2. Overview on our studies on diffusion in nanocrystalline materials. For an atomistic understanding of the diffusion process in nanocrystalline materials it is important to combine the given aspects.

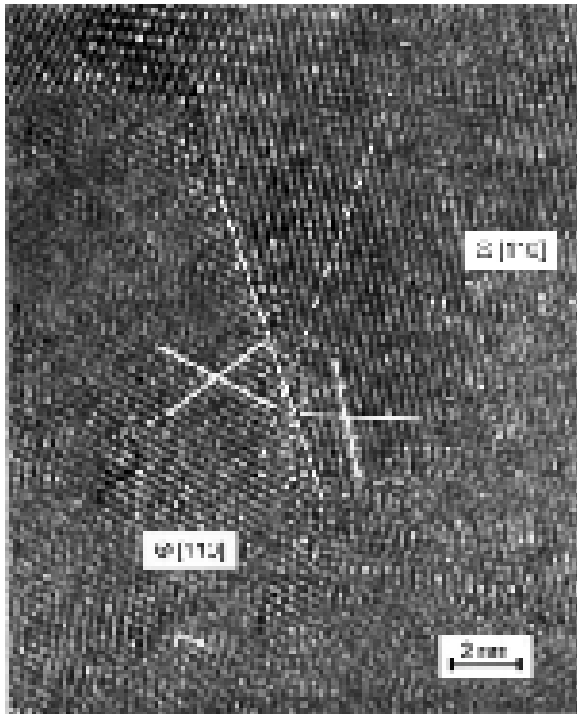


Fig. 4.3. Atomic resolution electron micrograph of nanocrystalline Pd exhibiting two adjacent crystallites with a $\Sigma 11$ orientation correlation. The orientation of the interface, however, entirely deviates from the direction of low-energy $\Sigma 11$ symmetric grain boundary.

the diffusion profiles of pure, unstabilized nanocrystalline ZrO_2 [87]. A profile can be separated between volume diffusion (diffusion in the crystallites) and grain boundary diffusion. Since ZrO_2 is used as an ion conductor of oxygen, it is of importance that oxygen diffuses much faster in the

grain boundaries than in the crystallites. An interesting experiment, which could be used to answer the question whether the fast diffusion is due to structural or thermal vacancy-like defects in the grain boundary, would be to measure the oxygen diffusion in nanocrystalline Y-stabilized ZrO_2 . Y causes the formation of structural oxygen-vacancies in the crystallites of coarse grained ZrO_2 .

Now, we report on the migration of atoms within the nanocrystallites in dependence on the state of order. This is also important for the material transport within the grain boundaries, because ordering could substantially change the volume diffusion constant and thereby the type of grain-boundary diffusion kinetics from type B to C. The preparation techniques for nanocrystalline materials, especially strong plastic deformations, offer the unique possibility to disorder bulk intermetallic alloys like FeAl which hardly can be disordered as coarse grained materials. Additionally, metastable, one-phase compositions, e.g. Al-rich FeAl, can be prepared.

Diffusion and ordering are closely correlated to each other. Both are governed by the migration of vacancies. The only difference is the distance over which the atoms migrate. For ordering a few jumps per atom should be enough to arrive at the correct lattice site so that the diffusion length after the ordering is about one lattice parameter (roughly 1 nm).

The ordering due to annealing of nanocrystalline, disordered FeAl, NiAl and Fe_3Si were measured by x-ray diffraction [90-93]. The mean temperature of ordering is ascribed to the temperature of 50% ordering. Fig. 4.5 shows the diffusion lengths for diffusion by thermal vacancies. It is evident that thermal vacancies account for the ordering in Fe_3Si [94],

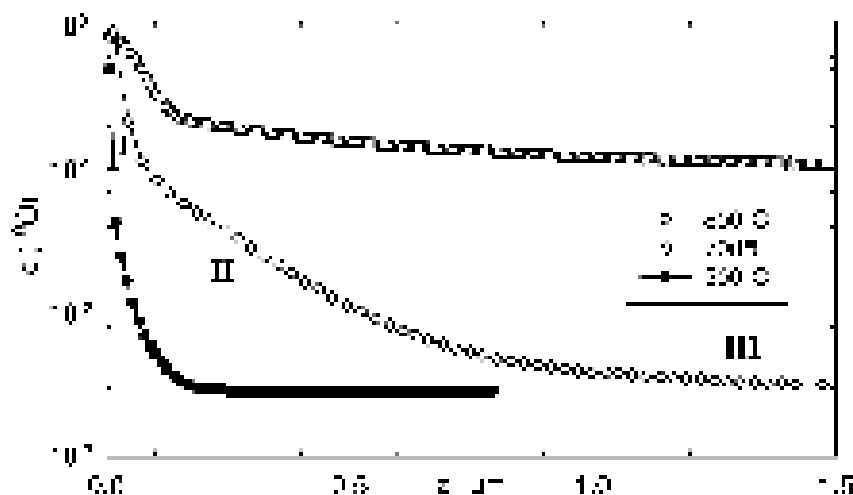


Fig. 4.4. ^{18}O diffusion profiles in undoped nanocrystalline ZrO_2 sintered at 950–970 °C to a relative mass density of 98% [87]. The profiles are typical for diffusion from a constant source in the type B regime. Three ranges of diffusion can be distinguished: diffusion (I) from the surface into the crystallites, (II) via grain boundaries, and (III) due to residual pores.

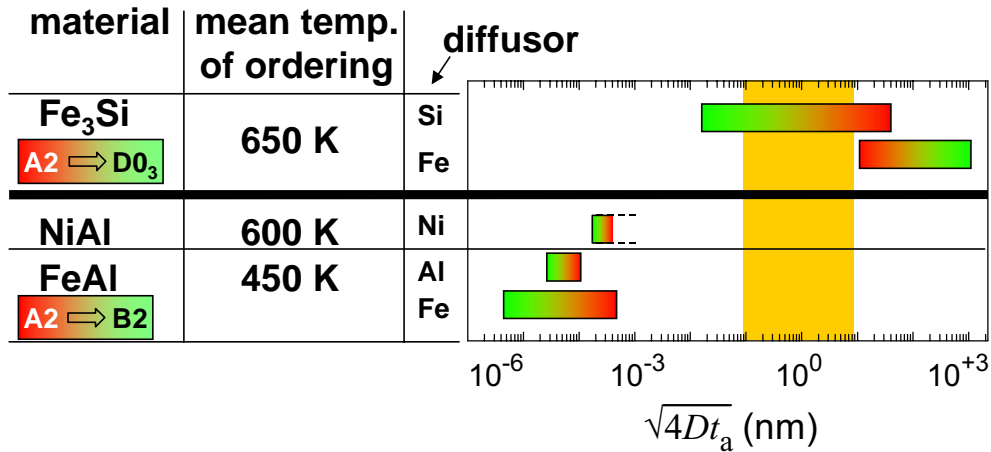


Fig. 4.5. The diffusion length $(4Dt_a)^S$ at the mean temperature of ordering were extrapolated or estimated from coarse grained materials [94]. For ordering by means of thermal vacancies the diffusion length should be about one atomic distance as indicated by the shaded region.

but the thermal vacancy concentration at the ordering temperature is much too small for ordering of FeAl and NiAl. Therefore we conclude that the ordering in FeAl and NiAl occurs by vacancies which were introduced during the preparation of the nanocrystalline alloys. Furthermore, these vacancies migrate faster in the disordered than in the ordered state [90], and they anneal out only after the ordering is complete. The reason for the annealing of vacancies in Fe₃Si before the ordering is complete originated from the low vacancy migration enthalpy on the Fe-sublattice [95].

In summary, we arrived at a consistent model of ordering and diffusion by means of vacancy migration for nanocrystalline [94,96] and coarse grained materials. This is a well defined starting point to separate the atomic migration in the crystallites and in the grain boundaries of nanocrystalline materials.

5. THEORETICAL MODELING OF GRAIN BOUNDARY DIFFUSION IN BULK NANOSTRUCTURED MATERIALS

5.1. Introduction

Nanostructured materials have become increasingly important both in fundamental and applied research because of their outstanding functional and structural properties; see, e.g. [97-106]. Of special interest, from both fundamental and application viewpoints, is the diffusion behavior of bulk nanocrystalline materials which, in general, is different from that of conventional coarse-grained polycrystals. Thus, following [1,81,98, 107-109], bulk

nanocrystalline materials exhibit the anomalously enhanced diffusional properties. For instance, the boundary diffusion coefficients in bulk nanocrystalline materials fabricated by high-pressure compaction and severe plastic deformation methods are several orders of magnitude larger than those in conventional polycrystalline materials with the same chemical composition [1, 81, 97, 107-109]. With these experimental data, the anomalously fast diffusion is treated as the phenomenon inherent to only nanocrystalline materials and is attributed to their specific structural and behavioral peculiarities [1, 97]. At the same time, however, there are experimental data indicating that the boundary diffusion coefficients in dense bulk nanocrystalline materials are lower than those measured in [107, 81, 108, 109] and similar to the boundary diffusion coefficients in conventional coarse-grained polycrystals or a little higher [75-78, 80]. These data form a basis for the viewpoint that the atomic diffusion in nanocrystalline materials is similar to that in conventional coarse-grained polycrystals. In doing so, the difference in the diffusivities between nanocrystalline and coarse-grained materials is treated to be related to only the difference in the volume fraction of the grain boundary phase. Thus, in general, there are controversial experimental data and theoretical representations on diffusion processes in nanocrystalline materials. Nevertheless, mechanically synthesized nanocrystalline bulk materials are definitely recognized to exhibit the enhanced diffusion properties compared to those of nanocrystalline materials fabricated by non-mechanical (more equilibrium than mechanical) methods and those of coarse-grained polycrystals;

see [81,108,109] and experimental results reported in this review. The experimentally documented phenomenon in question can be naturally explained as that occurring due to the deformation-induced non-equilibrium state of grain boundaries, in which case the grain boundary diffusivity highly increases. In this part of review we will consider theoretical models of diffusion processes in nanocrystalline materials with the special attention being paid to the role of non-equilibrium grain boundaries in the diffusion enhancement occurring in mechanically synthesized bulk nanocrystalline materials.

5.2. Theoretical models of diffusion in nanocrystalline materials. General aspects

Theoretical models of diffusion in nanocrystalline materials can be divided into the three following basic categories: (1) Models that describe grain boundary diffusion in conventional coarse-grained polycrystals and are directly extended to the situation with nanocrystalline materials, with nano-scale effects neglected. (2) Models focusing on the specific features of diffusion in nanocrystalline materials in the general situation, taking into account the nano-scale effects and neglecting the influence of preparation technologies on the structure and the diffusion properties of nanocrystalline materials. In short, such models deal with the “nanostructure-diffusion” relationship. (3) Models focusing on the structural and behavioral peculiarities of grain boundaries in nanocrystalline materials, taking into account the peculiarities of their fabrication. In short, such models are concerned with the “preparation-nanostructure-diffusion” relationship. Theoretical models of the first type and their application to a description of diffusion in nanocrystalline materials have been reviewed in detail by Larikov [72]. Such models are, in particular, those [110-114] describing spatial distributions of diffusing species within and near grain boundaries in polycrystals, models [115-123] focusing on microscopic mechanisms of grain boundary diffusion and models [123-131] dealing with diffusion-assisted processes (diffusional creep, diffusion-induced grain boundary migration, transformations of grain boundary dislocations and disclinations, etc.) in polycrystals. Now let us turn to a brief discussion of models describing the enhanced diffusion in nanocrystalline materials in the general situation, with the specific features of their preparation being neglected. In papers [132,133] it has been demonstrated that nano-

crystalline materials exhibit much larger variety of possible kinetic diffusion regimes compared to coarse-grained polycrystals. In particular, together with conventional A-, B- and C-regimes occurring in polycrystals [114], the additional diffusion kinetic regimes have been distinguished, depending on the grain size, diffusion temperature and time, the grain boundary segregation level in the case of impurity diffusion, and other parameters [133]. Also, as noted by Gleiter [1], the anomalously fast diffusion in nanocrystalline materials is related to the three following factors: (i) The diffusion in nanocrystalline materials is essentially enhanced due to the existence of high-density network of grain boundary junction tubes which commonly are characterized by more increased diffusion rate than grain boundaries themselves. (The highly enhanced diffusivity of triple junctions of grain boundaries is experimentally identified in polycrystals; see [134-138] and discussion in review article [139] concerning grain boundary junctions.) (ii) Rigid body relaxation of grain boundaries that occurs via relative translational displacements of their adjacent crystallites and reduces the boundary free volume is hampered in nanocrystalline materials. This is related to the fact that rigid body relaxation of the various boundaries surrounding every nanocrystallite require its different displacements due to their different atomic structure. (iii) In grain boundaries of nanocrystalline materials the concentration of impurities that often reduce boundary diffusivity is lower than that in grain boundaries in conventional polycrystals. Let us discuss factors (i)-(iii) in terms of Arrhenius formula for diffusivity in solids. The coefficient D of self diffusion occurring via transfer of vacancies¹ is given by the following Arrhenius relationship (e.g., [122,140]):

$$D = D_0 \exp\left[-\frac{\varepsilon_f + \varepsilon_m}{kT}\right], \quad (5.1)$$

where D_0 denotes the constant dependent on parameters of the ideal crystalline lattice, k is the Boltzmann's constant, T is the absolute temperature, ε_f and ε_m the energies of formation and migration of vacancies, respectively. In nanocrystalline materials (characterized by extremely high volume fraction of the grain boundary phase) self diffusion processes occur mostly via transfer of grain bound-

¹ In general, diffusion processes in crystals occur via transfer of point defects of different types. However, self diffusion occurring via transfer of vacancies is most effective; it is characterized by the largest coefficient of diffusion, e.g.[122,140].

ary vacancies. In these circumstances, all the factors (i)-(iii) discussed by Gleiter induce the characteristic boundary free volume to be increased and, as a corollary, both formation and migration of boundary vacancies to be facilitated in nanocrystalline materials as compared to those in conventional polycrystals. In terms of Arrhenius formula (5.1), the diffusion coefficient D is increased in nanocrystalline materials, because their characteristic energies, ε_f and ε_m , are decreased due to factors (i)-(iii) discussed in paper [1].

Now let us discuss theoretical models describing the enhanced diffusion in nanocrystalline materials fabricated at highly non-equilibrium conditions (say, by severe plastic deformation methods). Following [141-144], together with factors (i)-(iii) discussed by Gleiter [1], the existence and transformations of ensembles of grain boundary dislocations and disclinations strongly enhance diffusion processes in nanocrystalline materials fabricated at highly non-equilibrium conditions. The effects of such defects on diffusion are briefly as follows [143, 144]:

- (a) Disorderedly distributed grain boundary dislocations and disclinations are formed in nanocrystalline materials fabricated at highly non-equilibrium conditions. Such dislocations and disclinations re-arrange to annihilate or to form more ordered, low-energy configurations, in which case they move to new positions. Climb of (grain boundary) dislocations is accompanied by generation of new point defects [140, 145] – vacancies and interstitial atoms – serving as new carriers of diffusion. In this situation, generation of new vacancies occurs under the action of the driving force related to a release of the elastic energy of “non-equilibrium” grain boundary dislocations during their transformations. The action of the driving force in question facilitates diffusion processes in nanocrystalline materials. The effect discussed is quantitatively described by formula (5.1) with the sum $\varepsilon_f + \varepsilon_m$ being replaced by $\varepsilon_f - W_v + \varepsilon_m$, where $W_v (>0)$ is the energy release due to the climb of a grain boundary dislocation, per one vacancy emitted by the dislocation.
- (b) Cores of grain boundary dislocations and disclinations are characterized by excess free volume, in which case their presence in grain boundaries increases the total free volume that characterizes the grain boundary phase in nanocrystalline materials. This decreases values of ε_f and ε_m and, therefore, enhances diffusion processes occurring by vacancy mechanism.
- (c) Dilatation stress fields of grain boundary dislocations and disclinations influence migration of

vacancies. More precisely, in spirit of the theory of diffusion in stressed solids [146], the elastic interaction between vacancies and grain boundary dislocations and disclinations is characterized by the energy:

$$\varepsilon_{int} = -\frac{\sigma_{ii} \Delta V}{3}, \quad (5.2)$$

where σ_{ii} denotes the sum of dilatation components (say, components σ_{xx} , σ_{yy} , σ_{zz} , written in (x, y, z) – coordinates) of stress fields created by grain boundary defects, and ΔV the excess free volume associated with a vacancy. To minimize ε_{int} , vacancies migrate to regions where compressive stresses exist. This vacancy migration contributes to the enhanced diffusion in nanocrystalline materials. The effect discussed is quantitatively described by formula (5.1) with the sum $\varepsilon_f + \varepsilon_m$ being replaced by the sum $\varepsilon_f + \varepsilon_m + \varepsilon_{int}$.

Thus, the factor (a) gives rise to the diffusion enhancement owing to the influence of grain boundary dislocations on the generation of vacancies. The factors (b) and (c) facilitate the vacancy migration and therefore, cause the diffusion enhancement in nanocrystalline materials. According to the theoretical analysis [143], the most essential contribution to the diffusion enhancement is due to the dislocation climb in grain boundaries (see factor (a)). With this taken into account, in next section we, following [143, 144], will consider the effects of grain boundary dislocations on diffusion in nanocrystalline materials, with focusing on the climb of grain boundary dislocations composing dipole configurations.

5.3. Climb of grain boundary dislocations and diffusion in nanocrystalline materials

Nanocrystalline materials are effectively fabricated by mechanical methods at highly non-equilibrium conditions (see, e.g., [105, 147] and this review), in which case “non-equilibrium” defect structures are formed at grain boundaries. In particular, grain boundaries in such materials contain not only geometrically necessary dislocations (that is, grain boundary dislocations associated with the mean boundary misorientation, e.g., [123]), but also the so called “excess” grain boundary dislocations (that provide local deviations of the boundary misorientation from its mean value and commonly are chaotically distributed along a grain boundary)

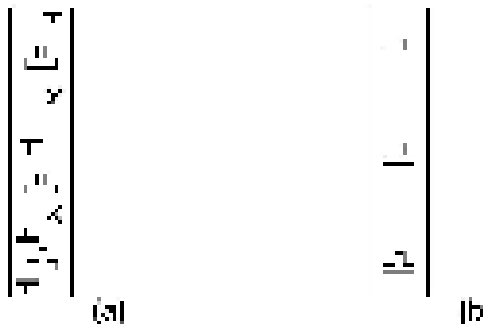


Fig. 5.1. Dislocation ensembles at (a) non-equilibrium and (b) equilibrium high-angle grain boundaries.

(Fig. 5.1a). In doing so, owing to highly non-equilibrium conditions of synthesis, the geometrically necessary dislocations at grain boundaries in mechanically synthesized nanocrystalline materials, in general, are disorderedly displaced relative to their “equilibrium” positions (Fig. 5.1a). During some relaxation time interval after mechanical synthesis of a nanocrystalline sample, transformations of the ensemble of grain boundary dislocations occur leading to a release of its elastic energy. In doing so, the “excess” dislocations with opposite Burgers vectors move (climb and glide) to each other and annihilate, and the geometrically necessary dislocations move (climb and glide) to their equilibrium positions (Fig. 5.1b).

The climb of grain boundary dislocations during the relaxation time interval is accompanied by both emission and absorption of point defects: vacancies and interstitial atoms (Fig. 5.2). In these circumstances, emission of vacancies (“take-off” of vacancies from dislocation cores and their consequent displacement into the surrounding grain boundary phase, see Fig. 5.2a) is more intensive

than that of interstitial atoms (Fig. 5.2b), because vacancies are essentially more mobile compared to interstitial atoms [140]. Also, it should be noted that absorption of vacancies, which accompanies the climb of grain boundary dislocations (Fig. 5.2c), needs vacancies to permanently move to dislocation cores from a surrounding material, while emission of vacancies (Fig. 5.2a) is not related to such a restrictive condition. As a corollary, emission of vacancies (Fig. 5.2a) occurs more intensively than absorption of vacancies (Fig. 5.2c) and absorption of slow interstitial atoms (Fig. 5.2d). With the aforesaid taken into account, in the following we will focus our consideration on the effects of only those processes of grain boundary dislocation climb, that are accompanied by emission of vacancies (Fig. 5.2d).

The largest contribution to energy of “non-equilibrium” defect structures at grain boundaries (Fig. 5.1a) commonly is related to the existence of excess grain boundary dislocations. Therefore, climb and annihilation of such dislocations, which are accompanied by emission of vacancies are characteristic processes of relaxation of grain boundaries in nanocrystalline materials. Below, for definiteness, we, following [143,144], will consider one of such processes, namely the climb and consequent annihilation of two grain boundary dislocations that compose a dipole configuration of the vacancy type (that is, dipole of dislocations whose annihilation results in emission of vacancies); see Fig. 5.3.

Stress fields of the grain boundary dislocations composing the dipole are effectively screened with the screening length λ being the dipole arm (distance between the dislocations; see Fig. 5.3a). Therefore, the energy W of the dislocation dipole, in the framework of the linear theory of elasticity (e.g., [145]), is given by the following approximate formula:

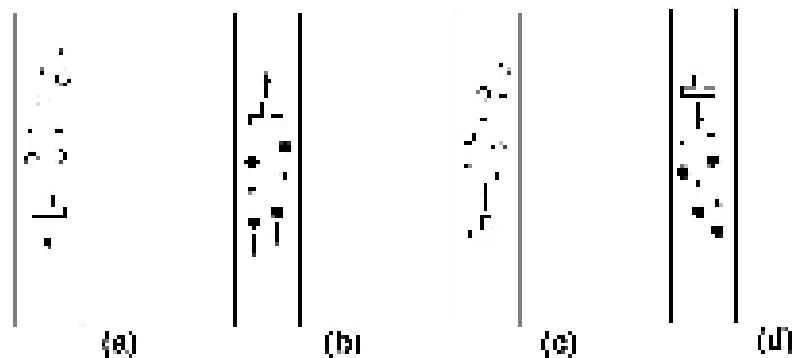


Fig. 5.2. Types of the climb of grain boundary dislocations.

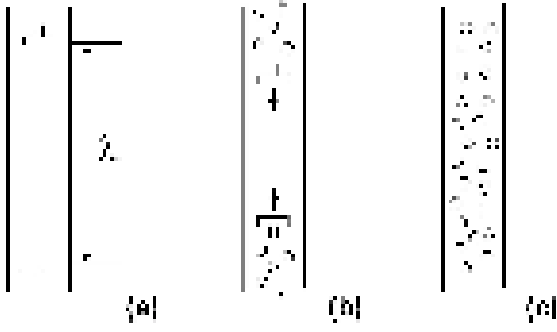


Fig. 5.3. Climb and annihilation of grain boundary dislocations composing dipole configuration.

$$W(\lambda) = 2W_d(\lambda) \approx \frac{Gb^2d}{2\pi(1-\nu)} \left(\ln \frac{\lambda}{r_0} + Z \right) \quad (5.3)$$

for $\lambda > 2a$. Here $W_d(\lambda)$ denotes the energy of dislocation having λ as the screening length of its stress field, d the dislocation length, $\pm b$ the dislocation Burgers vectors, G the shear modulus, ν the Poisson ratio, r_0 the dislocation core radius, Z the factor taking into account the contribution of the dislocation core into energy W .

Climb of one of the dislocations composing the dipole configuration by a , the mean interatomic distance in the grain boundary, (Figs. 5.3a and b) releases the dipole energy by value of $\Delta W(\lambda) = W(\lambda) - W(\lambda - a)$ and results in emission of d/a vacancies. In this situation, $\tilde{\epsilon}_f$, the energy of formation of one vacancy at the climb of the dislocations that compose the dipole configuration (Figs. 5.3a and b), is given as:

$$\tilde{\epsilon}_f = \epsilon_f - W_v(\lambda), \quad (5.4)$$

where ϵ_f is the energy of formation of one vacancy in the grain boundary phase in the absence of dislocations, and $W_v(\lambda)$ is the decrease of the dislocation dipole energy W due to emission of one vacancy, related to the climb of the dislocations composing the dipole:

$$W_v(\lambda) = \frac{a}{d} \Delta W(\lambda) = \frac{a}{d} (W(\lambda) - W(\lambda - a)) \quad (5.5)$$

for $\lambda > 2a$, from (5.4) and (5.5) we find

$$W_v(\lambda) = \frac{Gb^2a}{2\pi(1-\nu)} \ln \frac{\lambda}{\lambda - a}. \quad (5.6)$$

For $\lambda \leq 2a$, stress fields of the dislocations composing the dipole configuration, are localized mostly in dislocation cores, in which case the dis-

location energy is highly influenced by factor Z . The further climb of the dislocation towards each other represents, in fact, the process of their annihilation resulting in emission of $2(d/a)$ vacancies and decreasing the dipole energy from its value

$$W(\lambda = 2a) \approx \frac{Gb^2a(\ln 2 + Z)}{2\pi(1-\nu)} \text{ at } \lambda = 2a \text{ to zero that}$$

corresponds to $\lambda = 0$ (annihilation). As a corollary, for $\lambda \leq 2a$, the dipole energy decreases by value of

$$W_v(\lambda) \approx \frac{Gb^2a(\ln 2 + Z)}{4\pi(1-\nu)} \quad (5.7)$$

due to emission of one vacancy, which accompanies the dislocation annihilation.

The dependence of W_v on λ/a , given by formulae (5.6) and (5.7), is shown in Fig. 5.4, for the following characteristic values of parameters: $G=50$ GPa, $a \approx 0.3$ nm, $b \approx a/3$, $Z \approx 1$, and $\nu \approx 1/3$. From Fig. 5.4 it follows that emission of vacancies is facilitated more intensively with decrease of the distance λ between the dislocations composing the dipole configuration.

Let us discuss the effect of dislocation-climb-induced emission of vacancies on diffusion in nanocrystalline materials. The coefficient of diffusion occurring via vacancy mechanism (which commonly is most effective) in the absence of "excess" boundary defects is given by formula (5.1), where factor $\exp(-\epsilon_f/kT)$ characterizes equilibrium concentration of vacancies (when dislocation climb and dilatation stresses do not influence vacancy formation). The vacancy concentration in vicinity of the climbing dislocations (Fig. 5.3) is higher than the equilibrium concentration, because vacancy formation is facilitated due to the climb of dislocations. The effect in question is quantitatively described by the following change of the vacancy formation energy: $\epsilon_f \rightarrow \tilde{\epsilon}_f = \epsilon_f - W_v$ and by the corresponding local change of diffusion coefficient: $D \rightarrow D^*$, where D^* in vicinity of the climbing dislocations (Fig. 5.3) is given as:

$$D^* = D \exp\left(\frac{W_v}{kT}\right). \quad (5.8)$$

With the dependence $W_v(\lambda)$ (see Fig. 5.4) taken into consideration and factor $\exp(W_v/kT)$ averaged on λ (ranging from 0 to $10a$), we find that the diffusion coefficient in vicinity of the climbing dislocations is $D^* \approx 300 \cdot D$.

In nanocrystalline materials during relaxation time interval (after synthesis at highly non-equilibrium

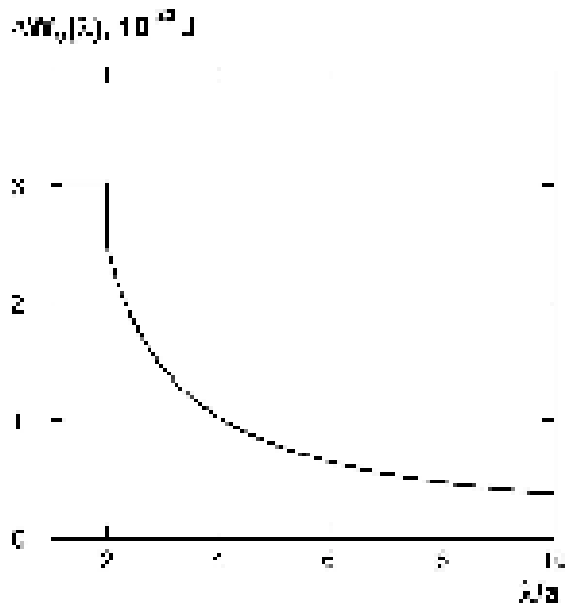


Fig. 5.4. Dependence of W_v on λa .

conditions, say, after fabrication by severe plastic deformation method) almost all grain boundaries contain non-equilibrium defect structures, in particular, “excess” dislocations whose annihilation enhances diffusion. In this situation, D' plays the role of grain boundary diffusion coefficient in nanocrystalline materials fabricated at highly non-equilibrium conditions. To summarize, our estimations allow us to conclude that the climb of grain boundary dislocations (Fig. 5.3) essentially enhances diffusion processes in nanocrystalline materials (in particular, nanocrystalline materials fabricated by severe plastic deformation), causing increase of the grain boundary diffusion coefficient by about 2 orders of magnitude. Thus, the climb of grain boundary dislocations is capable of strongly contributing to the experimentally observed (see [81,107-109]) anomalously fast diffusion in nanocrystalline materials during some relaxation time interval after their synthesis at highly non-equilibrium conditions.

Similar effects on the diffusion enhancement are caused by climb transformations of complicatedly arranged boundary dislocation structures (say, dislocation walls) in nanocrystalline bulk materials and films [148]. In doing so, misfit stresses (which commonly play the important role in processes occurring in single-, poly- and nanocrystalline films, e.g., [149-158]) essentially affect transformations of grain boundary defects and, therefore, the diffusion processes in nanocrystalline films [148].

Following [141-143], the elastic interactions between the diffusing species and grain boundary dis-

locations and disclinations (see point (c) in section 5.2) facilitate migration of vacancies and impurities, causing the diffusion enhancement in vicinities of grain boundaries. In this situation, the diffusion rate is increased by factor $M \sim 1-5$ in vicinities of grain boundaries. The effect discussed is small compared to that related to the climb of grain boundary dislocations.

5.3. Concluding remarks

Thus, there are controversial experimental data and theoretical representations on diffusion processes in nanocrystalline materials. At the same time, diffusion in mechanically synthesized bulk nanocrystalline materials is definitely recognized as the strongly enhanced diffusion compared to that in coarse-grained polycrystals and nanocrystalline materials fabricated by non-mechanical (more equilibrium than mechanical) methods. This experimentally documented phenomenon is naturally explained as that occurring due to the deformation-induced non-equilibrium state of grain boundaries, in which case mechanically generated grain boundary defects strongly enhance the boundary diffusivity.

6. RELATED PHENOMENA (GRAIN BOUNDARY PHASE PHENOMENA, SUPERPLASTICITY) IN NANOSTRUCTURED MATERIALS

The properties of modern materials, especially those of superplastic, nanocrystalline or composite materials, depend critically on the properties of internal interfaces such as grain boundaries and interphase boundaries (IBs). All processes which can change the properties of GBs and IBs affect drastically the behaviour of polycrystalline metals and ceramics [159]. GB phase transitions are one of the important examples of such processes [160]. Recently, the lines of GB phase transitions began to appear in the traditional bulk phase diagrams [160-165]. The addition of these equilibrium lines to the bulk phase diagrams ensures an adequate description of polycrystalline materials, particularly their diffusion permeability, deformation behaviour and the evolution of the microstructure.

In this work GB wetting, prewetting and premelting phase transitions are discussed. Consider the contact between a bicrystal and a liquid phase L . If the GB energy σ_{GB} is lower than the energy of two solid/liquid interfaces $2\sigma_{SL}$, the GB is not completely wetted and the contact angle $\theta > 0$. If $\sigma_{GB} > 2\sigma_{SL}$ the GB is wetted completely by the liquid

phase and $\theta = 0$. If the temperature dependencies $\sigma_{GB}(T)$ and $2\sigma_{SL}(T)$ intersect, then the GB wetting phase transition proceeds at the temperature T_w of their intersection. The contact angle θ decreases gradually with increasing temperature down to zero at T_w . At $T > T_w$ the contact angle $\theta = 0$. The *tie line of the GB wetting phase transition* appears at T_w in the two-phase region (S+L) of the bulk phase diagram. Above this tie line GBs with an energy σ_{GB} cannot exist in equilibrium with the liquid phase. The liquid phase forms a layer separating the crystals. Correct investigations of the GB phase transitions were performed using metallic bicrystals with individual tilt GBs in the Al–Sn [161], Cu–In [162], Al–Pb–Sn [161,166,167], Al–Ga, Al–Sn–Ga [168,169], Cu–Bi [163,170,171], Fe–Si–Zn [172–175], Mo–Ni [176], W–Ni [177] and Zn–Sn [165] systems. The tie-lines of the GB wetting phase transition were constructed basing on the experimental data [161,162,165–177]. The difference in the GB wetting phase transition temperature was experimentally revealed for GBs with different energies [162,166]. The precise measurements of the temperature dependence of the contact angle revealed also that the GB wetting phase transition is of the first order [166].

The deformation behavior of metals in the semi solid state has been extensively investigated from the viewpoint of rheological flow [179–180]. These studies have shown that the viscosity of the semi-solid metals depends on the volume fraction and morphology of the solid phase and the shear strain rate. In addition, the deformation behavior in a semi-solid state at the early stages of melting has been investigated by compressive creep tests [181–184]. Vaandrager and Pharr [182] showed that the deformation mechanism in a semi-solid state at the early stages of melting is grain boundary sliding accommodated by cavitation in a liquid phase for the copper containing a liquid bismuth. This deformation mechanism in the semi-solid state at the early stages of melting appears to be different from that in the semi-solid state during solidification. The presence of a liquid phase gives rise to complicated effects on the deformation behavior in the semi-solid state. Deformation in the semi-solid state is phenomenologically divided as follows; plastic deformation of solid phases, sliding between solid phases, flow of liquid incorporating solid phases and liquid flow [180]. For compressive deformation, because the liquid phase is squeezed out of boundaries experiencing compressive stresses in a very short time [182], it is difficult to investigate deformation related to the liquid flow by compressive tests. In [185] the shear

tests were carried out over a wide temperature range of 480–620 °C, including temperatures below and above the solidus temperature, for Al–5 wt. % Mg alloy to investigate deformation behavior in semi-solid states at early stages of melting. Pharr et al. [184] showed that the liquid phase significantly affects creep behavior of alloys when a significant portion of the grain boundary area, in excess of 70%, is wet. This revealed that the volume fraction of the liquid phase is an important factor in the deformation characteristics in the semi-solid state. The same trend has been reported in a semi-solid state at solidification [182]. However, deformation in the semi-solid state is very complicated and cannot be characterized only by the volume fraction of a liquid phase. In [185] the pure shear of Al–5 wt. % Mg alloy was investigated. This method permits to exclude the squeezing of the liquid phase from the sample. The shear strain to failure drops drastically at the solidus temperature (Fig. 6.1) [185]. In the semi-solid phase it is about 6 times lower than in the solid solution. Using the micrographs of the structure of polycrystals in the semi-solid state from [185] we calculated the fraction of the fully wetted GBs in dependence on the temperature. This dependence is shown in the Fig. 6.2. GB wetting phase transition proceeds in the Al–5 wt. % Mg alloy. The fraction of the fully wetted GBs increases with increasing temperature, and above $T_{wmax} = 892$ °C all high-angle GBs in the polycrystal are completely wetted. In the Fig. 6.3 the Al–Mg bulk phase diagram is shown with the lines of GB wetting phase transition (thin solid lines). The thick solid lines represent the bulk phase transitions [186]. Together with the tie-line of the full GB wetting at T_{wmax} , the tie lines at $T_{w0.75}$ and $T_{w0.5}$ are shown. They represent the temperatures, above which 75% and 55% of all high-angle GBs are wetted. The continuous change of the fraction of wetted GBs influences strongly the mechanism of the deformation. In Fig. 6.4 the temperature dependence of the shear strain rate is shown recalculated from the data [185]. In the solid solution the of the shear strain rate increases moderately with increasing temperature, and the activation energy (135 kJ/mol) is very close to the activation energy of Mg diffusion in Al (131 kJ/mol). In the semi-solid state the shear strain rate increases drastically. Close to T_{wmax} the (formally calculated) activation energy is about 1650 kJ/mol, i.e. ten times higher than the activation energy for the viscosity of Al melt. It means that in the semi-solid state no unique thermally-activated mechanism is working. Due to the temperature increase of the fraction of wetted GBs, the structure of the solid skeleton

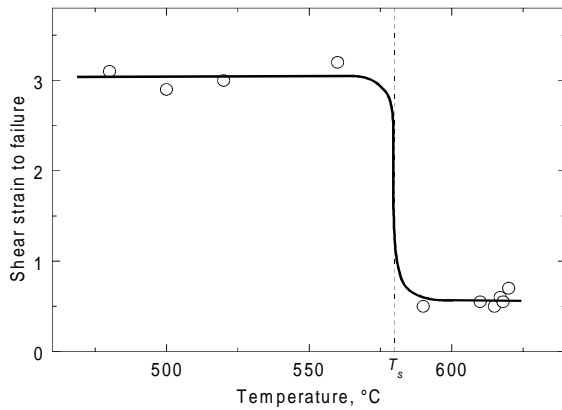


Fig. 6.1. Temperature dependence of shear strain to failure for Al – 5 wt. % Mg alloy in solid and semi-solid state [184].

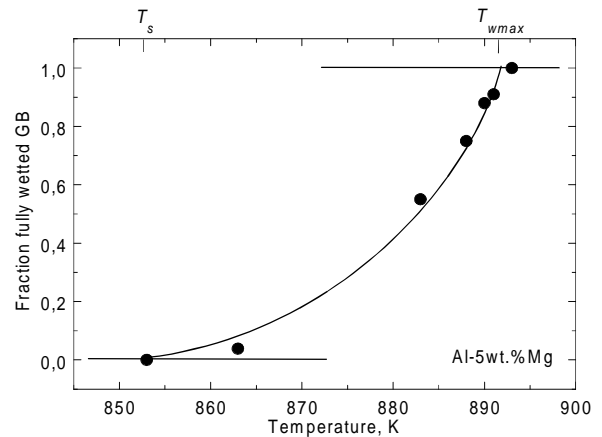


Fig. 6.2. Fraction of the fully wetted GBs in Al – 5 wt. % Mg polycrystals recalculated from micrographs published in [184].

changes continuously. It becomes more and more cutted with increasing temperature, therefore, making the shear easier in addition to the pure temperature activation.

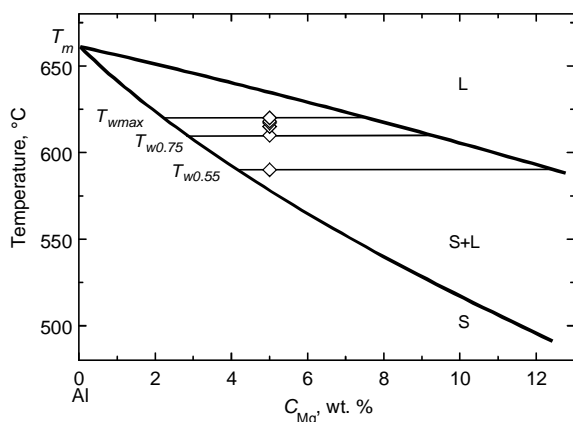
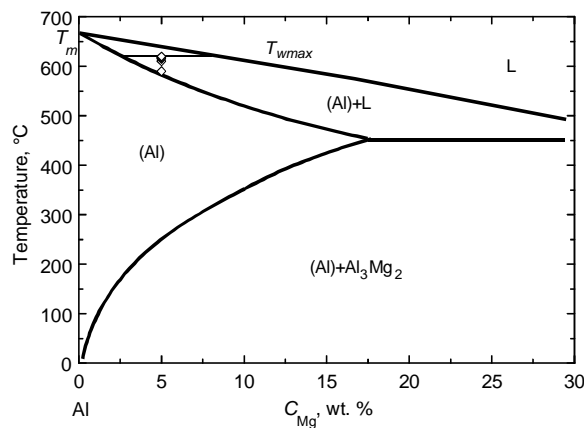


Fig. 6.3. Al–Mg phase diagram with the lines of bulk phase transitions (thick solid lines) and the tie – lines of the GB wetting phase transition (thin solid lines). In the enlarged part the tie-lines for the 50% and 75% wetted GBs are also shown.

It was pointed out by Cahn [187] that, when the critical consolution point of two phases is approached, GBs of one critical phase should be wetted by a layer of another critical phase, and in the one-phase region of a phase diagram there should be a singularity connected with an abrupt transition to a microscopic wetting layer. We distinguish two possible situations: the first one, when a layer of the new phase is formed on the GB (*prewetting transition*), and the second one, when the GB is replaced by a layer of the new phase (*premelting phase transition*). At the prewetting transition the difference between two phases must be small, while at the premelting transition the wetting phase may differ from that of the bulk dramatically. The lines of the GB prewetting or premelting phase transitions appear in the one-phase areas of the bulk phase diagrams where only one bulk phase can exist in the thermodynamic equilibrium (e.g. solid solution, see Fig. 6.5). These lines continue the tie-lines of the GB wetting phase transitions and represent the GB solidus (Fig. 6.5). The thin liquid-like layer of the GB phase exists on the GBs between the bulk solidus and GB solidus in the phase diagram. During the GB premelting phase transition this layer appears abruptly on the GB by the intersection of GB solidus. As a result, the GB properties (diffusivity, mobility, segregation) change dramatically.

The premelting transition has been revealed in the ternary Fe–Si–Zn system by measurements of Zn GB diffusivity along tilt GBs in the Fe–Si alloys [172–175]. It was found that the penetration profiles of Zn along GBs consist of two sections, one with a small slope (high GB diffusivity) at high Zn concentrations and one with a large slope (low GB diffusivity) at low Zn concentrations. The transition

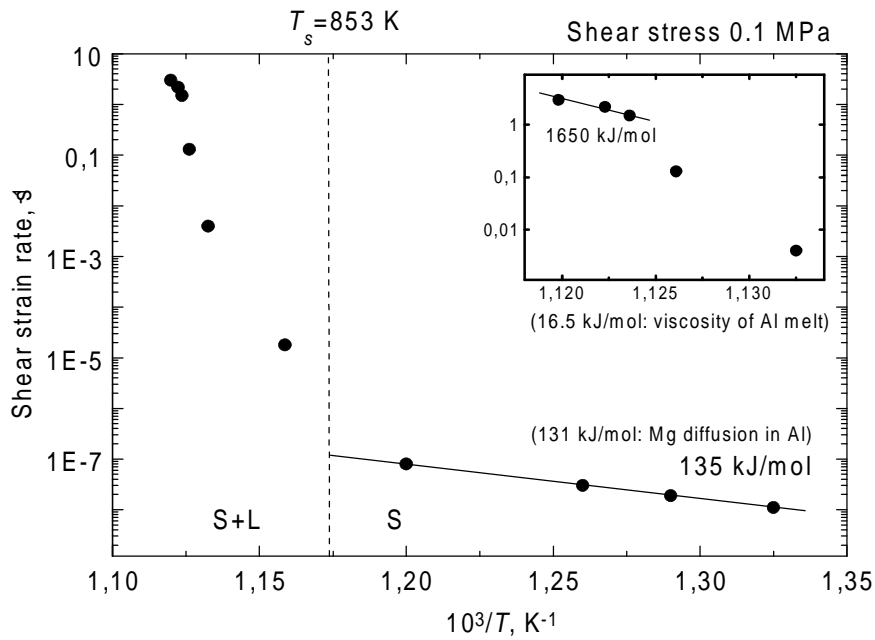


Fig. 6.4. Temperature dependence of shear strain rate for Al-5 wt. % Mg alloy in solid and semi-solid state (replotted from [184]).

from one type of behavior to the other was found to occur at a definite Zn concentration c_{bt} at the GB, which is an equilibrium characteristic of a GB and depends on the temperature (Fig. 6.6). The GB diffusivity increases about two orders of magnitude which is an indication of a quasi-liquid layer present in the GBs at high Zn concentration. The line of GB premelting phase transition in the one-phase area of the bulk phase diagram continues the line of the

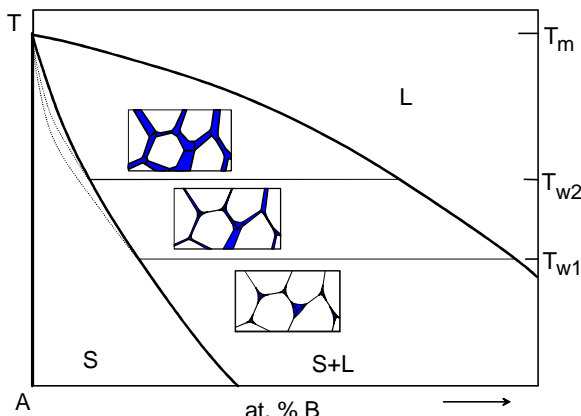


Fig. 6.5. Scheme of the phase diagram with lines of bulk and GB phase transitions. Thick solid lines represent the bulk phase transitions. Thin solid lines represent the tie lines of the GB wetting phase transition in the $S + L$ area for the high angle GBs having maximal and minimal possible energy. Thin dotted lines represent the GB premelting phase transition (GB solidus) proceeding in the area where only the solid solution is stable in the bulk.

GB wetting phase transition in the two-phase $L+S$ area: by pressure increase both the GB wetting and the GB enhanced diffusivity disappear together at the same pressure value (Fig. 6.7) [175]. The GB mobility was studied for two tilt GBs in bicrystals grown of high purity 99.999 wt. % Al and of the same material doped with 50 wt. ppm Ga [169]. The GB mobility increased about 10 times by increase of the Ga content for the both GBs studied. Normally, the addition of a second component can only decrease the GB mobility due to the solution drag [188]. The increase of the GB mobility can only be explained by the formation of the liquid-like Ga-rich

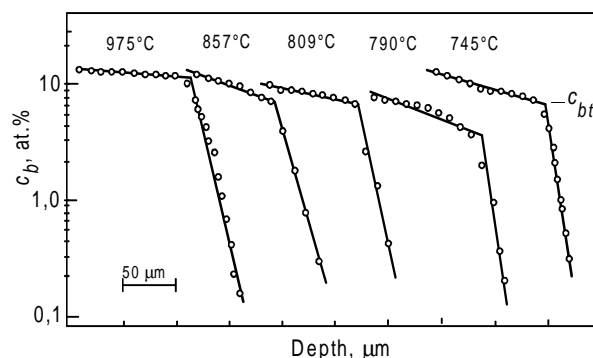


Fig. 6.6. Dependences of the GB concentration of Zn c_b on depth at various temperatures for the Zn GB diffusion in the Fe 5 - at. % Si bicrystal. c_{bt} is the GB solidus concentration where the GB diffusivity changes abruptly. c_{bt} is different at different temperatures. Above c_{bt} the GB diffusivity is high (liquid-like phase is present in GBs).

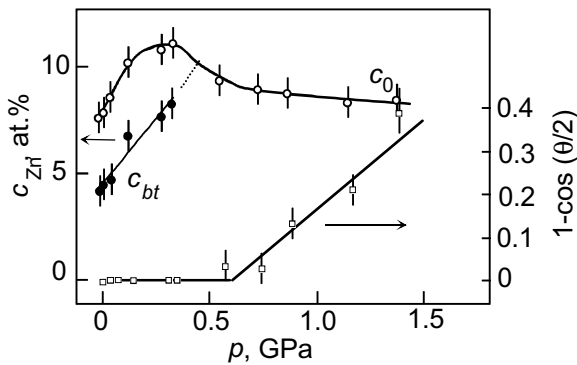


Fig. 6.7. Pressure dependence of the concentration of the bulk solidus (c_0), GB solidus (c_{bt}) and contact angle θ in the Fe – 5 at. % Si. Enhanced GB diffusion disappears simultaneously with GB wetting at $p = 0.5$ GPa [175].

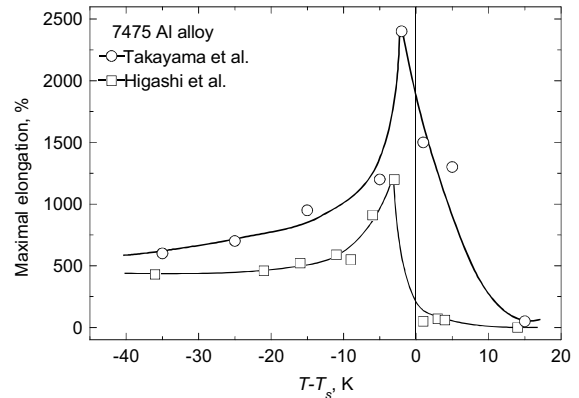


Fig. 6.9. The temperature dependence of the maximal elongation of the 7475 Al–Zn–Mg alloy samples. T_s is the solidus temperature. Circles represent the data [196] and squares are taken from [197].

layer on the GBs as a result of a premelting phase transition. The GB segregation of Bi in Cu was studied in the broad temperature and concentration interval [163,170,171]. It was shown that at a fixed Bi concentration the GB segregation change abruptly at a certain temperature (Fig. 6.8). Below this temperature the GB Bi concentration is constant and corresponds to a thin layer of pure Bi (GB phase). Above this temperature the GB segregation is lower than one monolayer of Bi and decreases gradually with increasing temperature according to the usual laws. These features indicate also the formation of a thin layer of a GB phase in the one-phase area of the bulk Cu–Bi phase diagram. The points of the abrupt change of the GB segregation form the GB solidus line in the bulk Cu–Bi phase diagram [170,171].

Superplastic forming is a commercial, viable, manufacturing technology. One of the major drawbacks of conventional superplastic forming is that the phenomenon is only found at relatively low strain rates, typically about 10^{-4} to 10^{-3} s $^{-1}$. Recently, a

number of studies have indicated that superplasticity can sometimes occur at extremely high strain rates (greater than 10^{-3} s $^{-1}$ and up to 10^2 s $^{-1}$). A specific example is a tensile elongation of over 1250% recorded at a strain rate of 10^2 s $^{-1}$ [188]. Thus far, this phenomenon, denoted as high-strain-rate superplasticity (HSRS), has been reported in several classes of materials, including metal alloys [189], metal-matrix composites [190-193] and mechanically-alloyed materials [194-196]. Despite these extensive experimental observations, the fundamental understanding of the factors leading to HSRS has not yet been arrived at. One very pertinent fact is that all of the materials that exhibit HSRS have a very fine grain size (~ 1 μ m). Another is that the phenomenon is observed at rather high homologous matrix temperatures and very close to the matrix solidus temperature. In Fig. 6.9 the example is shown of HSRS for the 7475 Al–Zn–Mg alloy. The data are taken from independent works [197,198] and reveal the very good reproducibility of the effect. Both temperature dependencies have rather

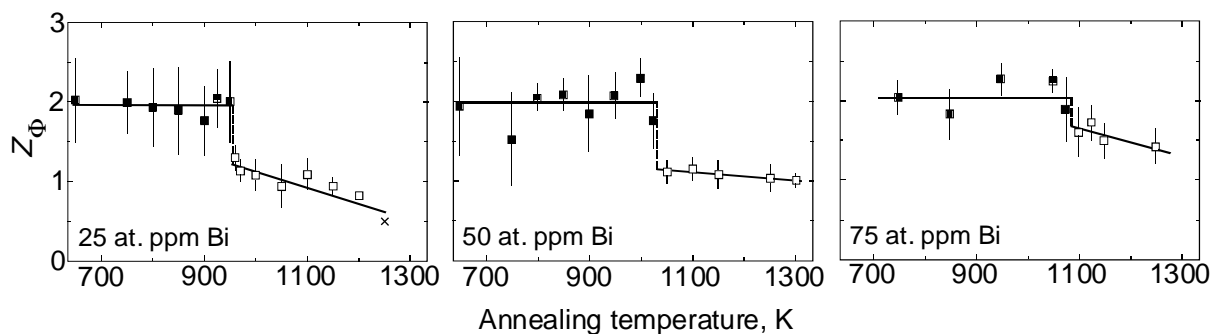


Fig. 6.8. Temperature dependence of the GB Gibbsian excess of Bi in Cu(Bi) polycrystals of various compositions, measured by AES. The sudden change of the GB segregation corresponds to the intersection of GB solidus line.

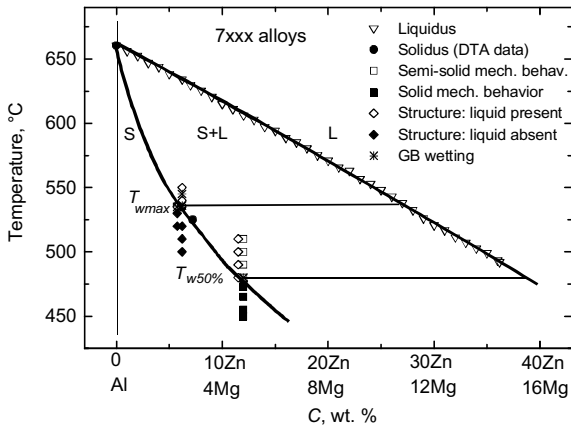


Fig. 6.10. The phase diagram containing the GB wetting phase transition tie-lines constructed for the 7xxx Al–Zn–Mg alloys.

narrow maximum few degrees below the solidus temperature T_s . It is important to mention that the solidus temperature was measured by the differential thermal analysis (DTA) in the same works [197,198]. The maximum elongation to failure reaches 1250%. Below T_s the maximal elongation is about 500%, above T_s , the maximal elongation drops very quickly down to almost 0%.

We suppose that the HSRs phenomenon can be explained using the ideas on the GB phase transitions in the two-phase S+L area and the solid solution area of the bulk phase diagrams. Using the data published in the literature, we constructed the lines of the GB wetting phase transition for the 7xxx Al–Zn–Mg alloys (Fig. 6.10). The liquidus line (thick solid line, open down triangles) have been constructed using the linear interpolation of liquidus lines for the binary Al–Mg and Al–Zn phase diagrams [186]. Solidus line (thick solid line, full circles) has been drawn through the melting point for Al [186] and experimental points obtained using DTA for the 7xxx alloys [183, 197-199]. Open and full squares mark the solid and semi-solid mechanical behavior, respectively [183]. Open and full diamonds mark the samples where the microstructural observations revealed the presence or absence of the liquid phase, respectively [183,197,198]. The analysis of the microstructures published in [183,197,198] permitted us to estimate the fraction of completely and partially wetted GBs (data marked by stars). These estimations allow to construct the GB wetting transition tie-lines (thin solid lines) for the T_{wmax} (above T_{wmax} all high-angle GBs in the polycrystal are completely wetted) [197,198] and $T_{w50\%}$ (above $T_{w50\%}$ about 50% of the high-angle GBs in the polycrystal are completely wetted) [183].

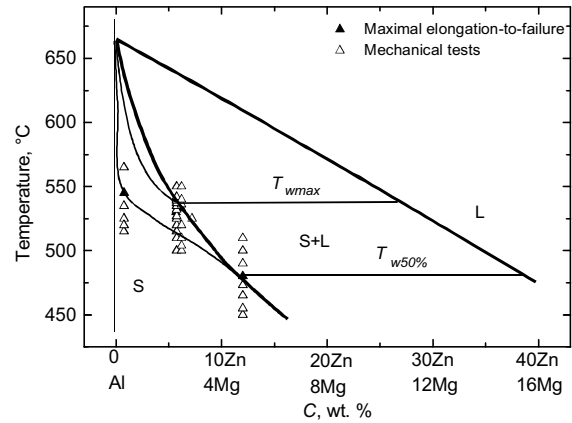


Fig. 6.11. The phase diagram containing the GB wetting phase transition tie-lines and GB solidus lines constructed for the 7xxx Al–Zn–Mg alloys.

In the Fig. 6.11 the liquidus, solidus lines and GB wetting tie-lines obtained in the Fig. 6.11 are repeated without experimental points. The data on mechanical tests (full and open up-triangles) are added [197-201]. Full triangles mark the maximal elongation-to-failure obtained in the tests performed at different temperatures [197,198,200]. Full triangles lie either below the bulk solidus line or coincide with it. The temperature difference between temperature of the maximal elongation-to-failure and T_s decreases with increasing concentration of Mg and Zn. According to the thermodynamics, the tie-lines of the GB wetting phase transition cannot finish at the intersection with the bulk solidus. They have to form the GB solidus line which continue in the solid solution area of the bulk phase diagram and finish in the melting point of the pure component. In the limiting case the degenerated GB solidus coincide with the bulk solidus. But in some systems it can extend into the solid solution area like it is shown in Fig. 6.7. In that case the layer of the liquid-like GB phase exists in the GBs between the GB and bulk solidus lines. Previously we have shown that the presence of such liquid-like layer in GB leads to the enhanced GB diffusivity, mobility and segregation of the second component [163,169-175]. Such GB solidus lines are drawn also in Fig. 6.11 (thin solid lines). They continue the T_{wmax} and $T_{w50\%}$ GB wetting tie-lines and finish in the melting point of Al. The GB solidus lines are drawn in such a way that the points of the maximal elongation-to-failure are between the GB and bulk solidus. Therefore, the enhanced plasticity of the nanograined polycrystals can be explained by the GB phase transition leading to the formation of the liquid-like layer on the GB in the narrow band of the solid solution area, just below the bulk solidus line. The phase diagrams

similar to those shown in Figs 6.10 and 6.11 can be constructed using the published data on HSRS, DTA and microscopy also for the 2xxx (Al–Zn–Mg) [192,184-196, 198, 202-204], 5xxx (Al–Mg) [194,198, 205,206] and 6xxx (Al–Si–Mg) [193,194,198,205-210] alloys. All authors studied the HSRS phenomenon mention that the physical reason of such a huge and reproducible increase of the plasticity is unknown. We suppose for the first time that the HSRS phenomenon can be explained by the existence of the equilibrium GB liquid-like layer close to the bulk solidus.

7. ORDERING-REORDERING KINETICS IN Ni_3Al BASE ALLOYS PROCESSED BY BALL MILLING

7.1. Introduction

Mechanical alloying (MA), first developed in the 1960s, is a high energy ball milling process [211-214]. An initial blend of powders is repeatedly kneaded together and re-fractured by the action of the ball-powder collisions until a powder is produced in which each particle has the composition of the initial powder blend. The extremely fine grain sizes generated during MA as well as the ability to produce a variety of non-equilibrium phases ranging from supersaturated solid solution to nanocrystalline and/or amorphous phases, may offer a means of improving ductility and providing a better balance of properties in challenging new materials, such as intermetallic compounds. Since the process takes

place entirely in the solid state, it is also possible to produce new alloys from virtually immiscible components. Alternatively the MA process can be used to distribute a second phase homogeneously throughout a chosen matrix to produce a particulate reinforced metal matrix composite (MMC).

Unlike other methods (phase gas composition, electrodeposition), mechanical alloying / ball milling (MA/BM) produces nanostructured materials not by cluster assembling but by structural decomposition of coarse-grained structures as the result of heavy plastic deformation. This makes BM technique similar to several plastic deformation techniques developed in [215]. Ball milling has become a widely used method to synthesize nanocrystalline materials because of its simplicity, the relatively inexpensive equipment and the applicability to essentially all classes of materials. Nevertheless, some serious problems are usually cited: contamination from milling media and/or milling atmosphere and the need to consolidate the powder product with maintaining the nanostructured feature of the material.

7.2. Ball milling devices

A variety of different types of ball mills have been used for the mechanical processing of powders, including attritor, vibratory mills and planetary mills. Fig. 7.1a shows the schematic view of an attritor [212]. Milling occurs by the stirring action of an agitator that has a vertical rotating shaft with horizontal arms. The motion causes a differential movement between the balls and the powder.

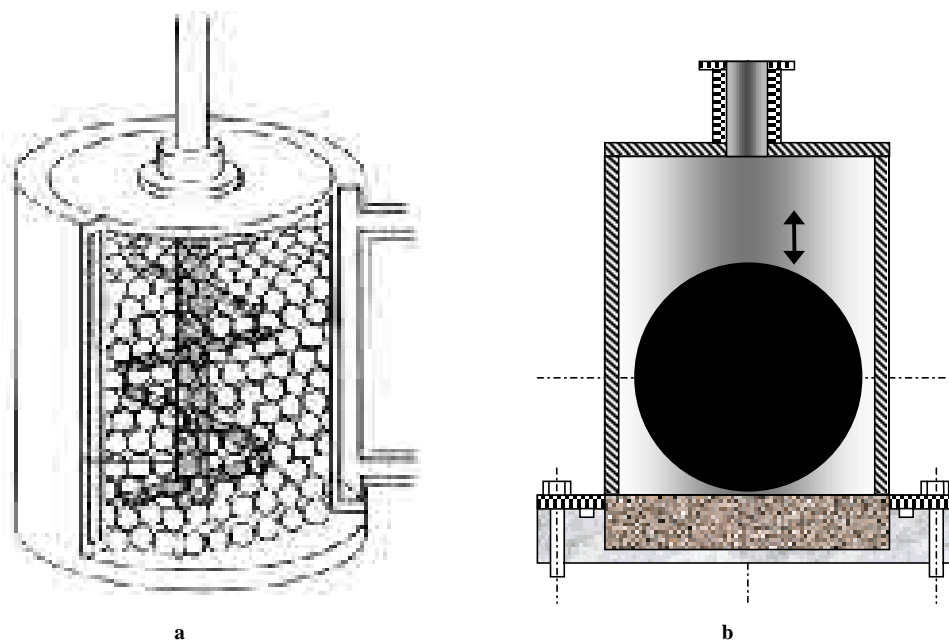


Fig. 7.1. Schematic view of high energy attritor-type ball mill (a) and of a vibratory mill (b).

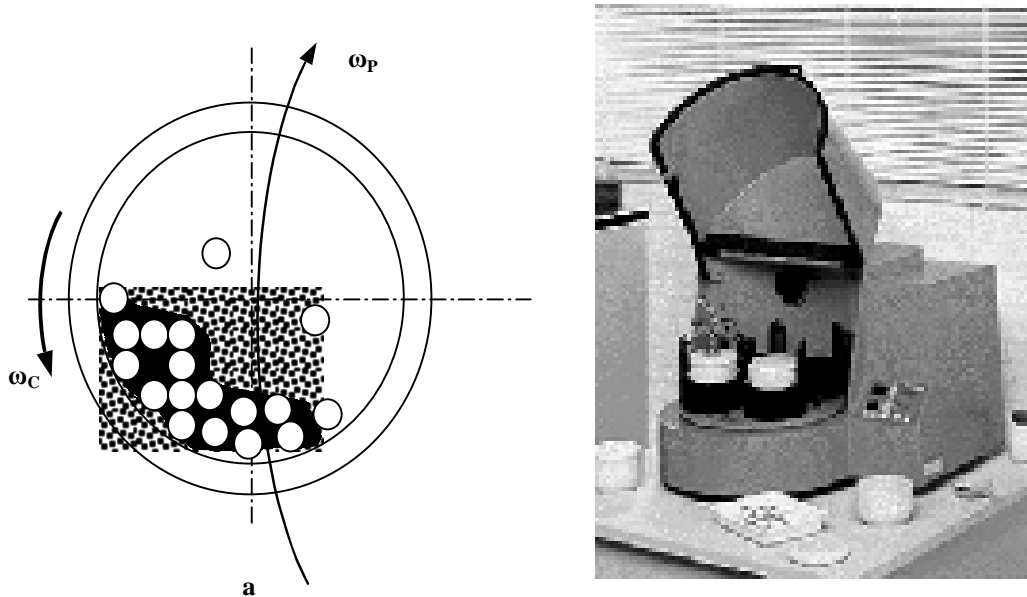


Fig. 7.2. Scheme of planetary mill (a) and external view (b).

Several different kinds of laboratory-scale high energy ball mills have been developed for research purposes. The SPEX model 8000 shaker has been used intensively for research on small amount of powder. The shaker is highly energetic compared to the attrition and vibratory mills [216]. Some of researchers have designed their own high energy milling devices. For example, the single large ball from steel vibrates in a tungsten carbide bottom steel vial attached to vibrating frame (Fig. 7.1b). To protect the sample against oxidation during milling, a turbomolecular high-vacuum system is usually connected to the ball-mill machine. Milling times can be varied from several minutes up to months. Fig. 7.2 demonstrates the scheme and photograph of planetary mill. This mill, also known as centrifugal or planetary mills, is a device used to rapidly grind materials to colloidal fineness (approximately 1 micron and below) by developing high grinding energy via centrifugal and/or planetary action. Each bowl sits on an independent rotatable platform, and the entire assembly is also rotated in a direction opposite to the direction of the bowl platform rotation. In planetary action, centrifugal forces alternately add and subtract. The grinding balls roll halfway around the bowls and then are thrown across the bowls, impacting on the opposite walls at high speed. Grinding is further intensified by interaction of the balls and sample. Planetary action gives up to 20 g acceleration and reduces the grinding time to about 2/3 of a simple centrifugal mill (one that simply spins around). Grinding media are available in agate, sintered corundum, tungsten carbide, tempered chro-

mium steel, stainless steel, zirconium oxide, and polyamide plastic. The exact type of bowl and balls that are used depend on the type of material being ground.

7.3. Kinetic of ordering – reordering transformation in Ni_3Al alloys

The main driving force for the study and development of advanced ordered alloys and intermetallics is the potential that this class of materials offers for high temperature applications. For this reason, in the last years, a considerable amount of work has been done to investigate ordered alloys. In the case of $L1_2(\gamma')$ alloys, they usually undergo a first-order transformation to a disordered fcc (γ) phase when heating beyond a critical transition temperature T_{cr} . The properties of both the ordered γ' and disordered γ phases as well as the thermodynamics and kinetics of the order-disorder transformations at T_{cr} can be studied by various techniques when T_{cr} is below the melting temperature T_m of the alloy [217]. However, $L1_2$ phases present an inaccessible equilibrium disordered γ phase, because $T_{cr} > T_m$, and in spite of an inadequate ambient temperature ductility and consequently, a limited workability, this class of materials have a great interest for industrial application due to their high temperature strength, relatively high melting points, and more oxidation and corrosion resistance [218,219].

It has been proved, that the lack of atomic order corresponds to an increase in the deformability in comparison to the ordered state, so it is certainly

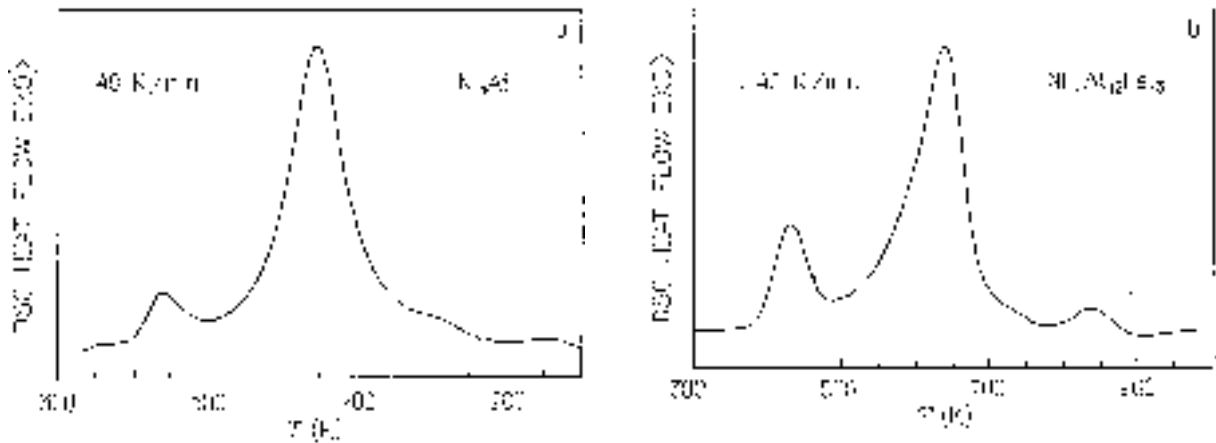


Fig. 7.3. DSC curve from Ni₃Al based alloy milled for 4 hours (a) and from Ni₇₅Al₁₂Fe₁₃ alloy milled for 8 hours (b).

interesting to understand how the disordered phase can be obtained and retained at room temperature. The discovery that permanently ordered phases can be completely disordered not only by intense plastic deformation [220,221], but also by electron irradiation [222] and, very recently, by ultra-rapid solidification of sputter deposited films and by melt-spinning [223], offers the possibility for a better understanding of how the physical and mechanical properties of such artificially disordered nanocrystalline alloys change as order is gradually reintroduced.

7.4. Experimental Procedure

The metastable nanocrystalline completely disordered Ni₃Al based alloys were prepared by mechanical attrition following the procedures described in [224,225], for Ni₃Al and Ni₇₅Al₁₂Fe₁₃ alloys, respectively. The x-ray diffraction (XRD) analysis was used for evaluating the average size of the coherent diffracting domains and the microstrain. More details can be found elsewhere [226]. The thermal stability of the metastable nanophase formed during ball milling was studied by differential scanning calorimetry (DSC) under pure argon atmosphere. Experimental details are described in [226]. Low temperature magnetic properties were measured using a superconducting-quantum interference device (SQUID) and high temperature measurements were performed on a furnace-equipped magnetometer [224].

7.5. Results and Discussion

Differential scanning calorimetry. On heating the milled samples, reordering, accompanied by grain

growth of the crystalline phase is observed. The DSC curves reported in Fig. 7.4 show a typical result of a continuous heating experiment on the samples studied. Independently of the composition, an exothermic transformation occurs over a wide range of temperatures (373-873K). This transformation is composed of different processes, as evident from the complex shape of the calorimetric signal. Similar results were obtained in ball milled Ni₃Al [220] and also for Ni₃Al vapor-deposited thin films [228]. It is interesting to compare DSC curve for Ni₃Al based alloy processed by severe plastic deformation techniques (Fig. 7.4) [229]. This suggests that reordering of these compounds is not affected by the way in which the metastable disordered nanocrystalline structure is achieved, and indirectly confirm, also for Ni₃Al, the analogies between metastable and nanocrystalline structures produced by mechanical attrition and other techniques, such as electrodeposition or severe plastic deformation [230]. All these transformations are irreversible: on repeating a heating DSC scan with the same specimen, no transformation was detected anymore. These second scans, performed without changing the sample configuration, were then used as baseline for estimating the total enthalpy output, from the integrated area of the peaks. The enthalpy release increases with the milling time and even long after long range order has disappeared, no evident steady value is achieved. In this sense, the contribution of grain growth to this enthalpy release cannot be disregarded. According to different authors [231,232] the enthalpic contribution coming from grain growth in nanocrystalline elemental powders shows values twice than expected for the enthalpy stored in the fully equilibrated grain boundaries of such a refined

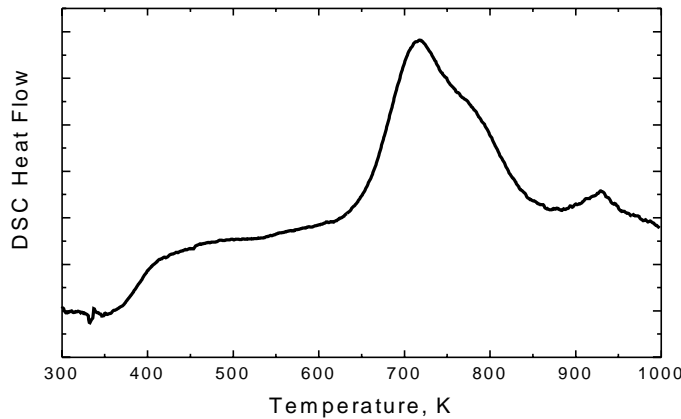


Fig. 7.4. DSC curve for Ni_3Al based alloy (Ni-8.5Al-7.8Cr-0.02B; in wt%) processed by high-pressure torsion.

microstructure. In this case approximately 60% of the enthalpy release can correspond to grain growth. Identification of the processes which may contribute to the complex calorimetric signal has been attempted and reported elsewhere [224]. Three stages have been identified, the second, more intense signal being associated with the simultaneous evolution of ordering and grain growth. This result is again in agreement with those already reported for both milled powders [220] and thin films [228].

Harris et al. [228] regard the low-temperature peak as determined by the reestablishment of short-range order. This hypothesis is nicely proved by the results obtained from electron energy-loss fine structure measurements on Ni_3Al thin films, vapor-deposited in the disordered nanocrystalline state, and then annealed for several hours at 423K [233]. A further proof of such attribution of the low temperature exothermic peak to short-range reordering is indirectly given by the DSC curves reported for elemental milled powders [234]. They show in fact a complex exothermic process very similar to those observed for our milled powders. The only substantial difference is the lack of the low temperature peak that, in view of its suggested origin, cannot be present as no chemical reordering can occur in pure metal powders. No clear and conclusive interpretation is proposed for the high temperature, weaker component of the overall transformation. It is also the more difficult phenomenon to deal with, since it strongly overlaps the second process. By considering the temperature range over which it occurs and the low enthalpy associated with it, it can be inferred that it might be due to annealing out of dislocations, usually not mobile at temperatures as low as those of the first two processes. Against this dislocation related interpretation are the already mentioned observations reported for Ni_3Al nanocrystalline thin-

films. As said, the structure of the DSC curves is exactly the same as that of the milled powders. It is difficult to figure out the reason why a high density of dislocations should be present in these thin films in such a concentration to affect their reordering kinetics.

Magnetic measurements. The low-temperature magnetization curves at an intensity field of 2 kOe are shown in Fig. 7.5 where Fig. 7.5a corresponds to the disordered state of a nanocrystalline Ni_3Al based alloy and Fig. 7.5b to the same sample annealed to restore the $L1_2$ ordered phase. From the figure it is seen that the Curie temperature of both phases is about 85K, while the magnetization at very low temperature of the γ phase is much higher than that of the disordered phase. While the γ state of Ni_3Al is ferromagnetic only at low temperatures, the addition of a few percent of Fe raises the Curie temperature T_c very rapidly to several hundred degrees as giant moments around Fe-atoms polarize the surrounding nickel atoms [235]. Fig. 7.6 shows the magnetization at an intensity field of 2 kOe versus temperature for $\text{Ni}_{75}\text{Al}_{12}\text{Fe}_{15}$ disordered for 8 h by ball-milling. Due to the disorder to order transition the heating curve is irreversible but the cooling curve is superimposed by subsequent heating and cooling cycles.

Kinetics evaluated from DSC Measurements. Kinetic analysis based on calorimetric measurements has been performed on the second contribution to the exothermic peak of a sample which was milled for 20 h. The kinetic analysis of the reordering process has been done in terms of the transition state rate theory, which properly describes the kinetics of many thermally activated solid-state reactions. For this purpose, the fraction transformed, x , and its rate, dx/dt , have been determined for the different DSC experiments as reported in [235]. In

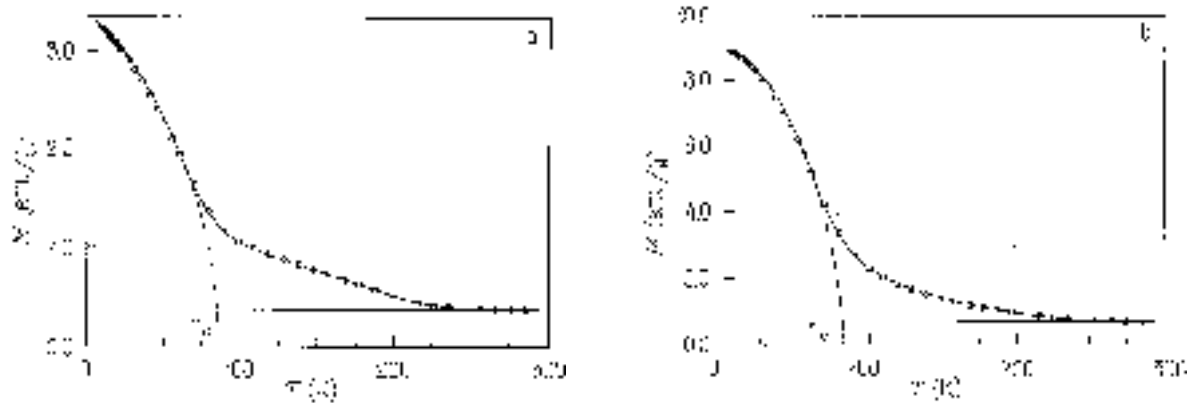


Fig. 7.5. Low-temperature magnetisation of disordered Ni₃Al based alloy after 4 h ball-milling (a) and same alloy subsequent annealed to re-establish L₁₂ ordered phase (b). Applied field 2 kOe.

the classical nucleation-and-growth process, as depicted by the Johnson-Mehl-Avrami-Erofe'ev (JMAE) analysis [236], the rate of transformation is given by

$$\frac{dx}{dt} = K(t)f(x). \tag{7.1}$$

Here $K(T)$ is the reaction rate, generally given by an Arrhenius expression

$$K(t) = K_0 \exp\left(-\frac{E}{RT}\right), \tag{7.2}$$

where E is also the apparent activation energy and K_0 the pre-exponential factor both independent of temperature or progress of the transformation provided if the temperature range, over which the transformation occurs, is not too broad. The function $f(x)$ is given by the expression

$$f(x) = p(1-x)[-\ln(1-x)]^{\frac{p-1}{p}}, \tag{7.3}$$

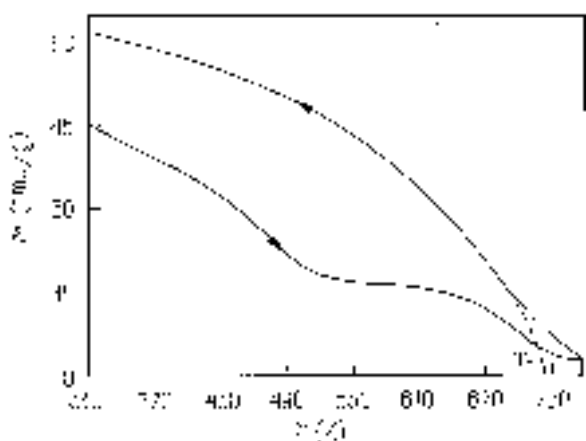


Fig.7.6. Magnetization of disordered Ni₇₅Al₁₂Fe₁₃ vs. temperature. Applied field 2 kOe.

where p is the kinetic exponent that, depending on the nucleation mechanism and growth morphology, varies p between 0.5 and 4 [237]. Under continuous heating (at a constant rate β) Eq. (7.1) can be rewritten as

$$\frac{dx}{dT} = \frac{k(t)f(x)}{\beta}. \tag{7.4}$$

There are many different types of processes whose to transformation behavior could be described by the general kinetic Eqs. (7.1) to (7.4) in a certain range of temperature.

The study of the reordering kinetics was carried on a sample ball-milled for 20 h and the values of the kinetic parameters E , K_0 and p were calculated from experimental data. The Kissinger's plot [238] was used to evaluate the apparent activation energy, E . The values of E obtained in this way for the reordering process, remain constant irrespective of the milling time, within the experimental errors [223]. Similar values of E have been obtained for all the samples analyzed, irrespective of the their composition. The other parameters have been determined by best fitting the simulated calorimetric DSC signal to that can be deduced from the model to the experimental DSC signal of the reordering process of the sample studied. The results are quoted in Table 7.1.

Fig. 7.7 shows the DSC curve, at 40 K/min, corresponding to the reordering peak together with the best fit obtained by the JMAE theory. Further confirmation of the ability of the considered models to reproduce the experimental behavior is found by comparing continuous heating experiments, performed at different heating rates, to the corresponding simulations. An example of this is given in Fig. 7.8 where the DSC curves taken at two

Table 7.1. Values of the kinetic parameters obtained: a) from DSC measurements; b) from magnetic measurements [225].

| | E (eV) | K_0 (s ⁻¹) | p |
|--|------------|--------------------------|-------|
| Ni ₃ Al | a) 1.6 | $3 \cdot 10^{10}$ | 0.6 |
| Ni ₇₅ Al ₁₂ Fe ₁₃ | a) 1.7 | – | – |
| | b) 1.1-1.8 | – | 0.7-1 |

different heating rates are shown. Superimposed on them are the signals predicted by the JMAE model. The shift of the peak temperature is well reproduced. As well as in continuous heating regime, calorimetric results have been obtained by operating the DSC in isothermal regime. This is a usual procedure to extend the temperature range available to calorimetric measurements and thus to increase the precision in kinetic analysis. In Fig. 7.9 the isothermal DSC curves obtained at two different temperatures after heating from room temperature at a scanning rate of 40 K/min are presented. The curves simulated by the JMAE model are also shown. Two facts, however, prevented us from getting all information expected from these isothermal regime measurements. First, the signal is characterized by a continuous decay; second, at temperatures which correspond to the early stages of the contribution studied, and even after long annealing times (several hours), the process has not gone to completion, as is evidenced on further continuous heating. So, kinetic data available from isothermal

measurements can only be evaluated from continuous heating experiments performed before and after the anneals. Only in this way it is possible to know the extent at which the transformation has proceeded during the isothermal anneal. The anneals performed complete the transformation progressively and, as the annealing temperatures are low, the third contribution remains unchanged and causes little problem. The JMAE analysis fails to reproduce the calorimetric results observed upon isothermal annealing (Fig. 7.10). Correct reproduction has been obtained by using an increasing value for the apparent activation energy (from 1.42 to 1.85 eV) of the process [239].

Kinetics evaluated from magnetic measurements. The measured magnetization of Ni₇₅Al₁₂Fe₁₃ alloy corresponds to

$$M(T) = x_d M(\gamma, T) + x_o M(\gamma', T), \quad (7.5)$$

where x_d and x_o are the disordered and ordered fractions, respectively. During the isothermal annealing in the magnetometer, the magnetization evolves according to

$$M(T) = x_d M(\gamma, T_{iso}) + x_o M(\gamma', T_{iso}). \quad (7.6)$$

At temperatures higher than the Curie temperature for the disordered alloy, there is no magnetic signal from the disordered phase. So, one can say $M(T) = 0$ at $T > T_c(\gamma)$ and set the first term in equation (7.6) equal to zero and x_o could be evaluated through the following expression:

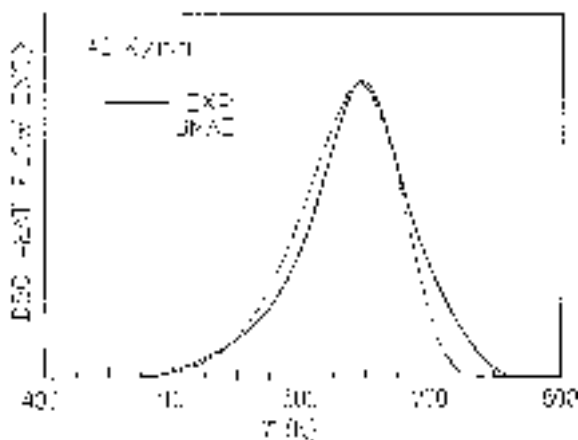


Fig.7.7. Enlarged view of the deconvoluted reordering peak from a sample milled for 20 h. The dashed line correspond to a simulation using Eqs. (7.3, 7.4).

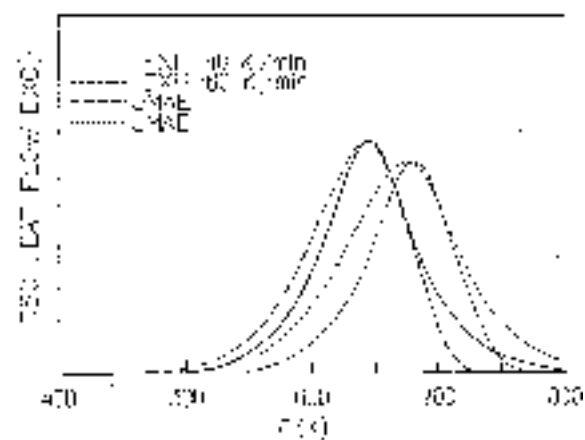


Fig. 7.8. Scanning calorimetry curves from Ni₃Al milled for 20 h. The dashed lines are simulations according to Eqs. (7.3, 7.4).

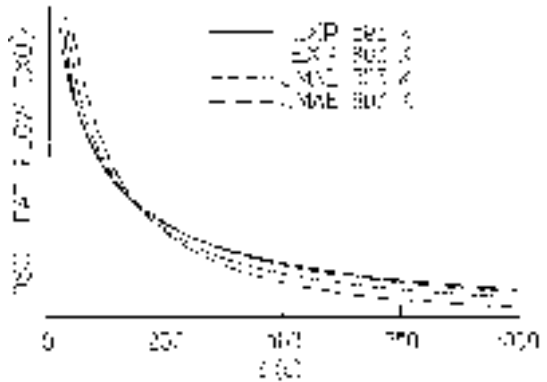


Fig.7.9. Isothermal DSC curves from Ni₃Al milled for 20 h compared to the calculated one from Eqs. (7.1, 7.3).

$$x_0 = \frac{M(T)}{M^0(\gamma', T_{iso})}, \quad (7.7)$$

where the denominator corresponds to the magnetization of the fully ordered γ' -state (with $x_0 = 1$) obtained from the cooling curves of the magnetization versus temperature at temperatures T corresponding to the isothermal annealing temperature T_{iso} .

To study the reordering kinetics, isothermal measurements of magnetization of disordered Ni₇₅Al₁₂Fe₁₃ alloy have been carried out. The ordered fraction has been evaluated taking into account the fraction already transformed when the isothermal annealing begins at time $t=0$. Isothermal measurements at successive temperatures were performed with the same sample, stepping up the temperature from T_1 to T_2 for example, after a time t_1 at T_1 . From the magnetic measurements the kinetic parameters E and p were evaluated and are quoted in Table 7.1. In [234] is argued that such low

exponents of the JMAE equation can be explained by assuming that the ordered phase nucleates inside each nanograin and cannot propagate from grain to grain. These observations may have further support from the results obtained in [226, 240]. We have found in fact that not only a lower limiting value of the long-range order parameter, but also that, after long term annealing, the ordered domain size coincides with the average size of the coherent, scattering domain, and the limiting value of the LRO parameter is still lesser than unity. As in the DSC study an increase in E was found with increasing temperature.

The increase which is observed in the values of the apparent activation energy with T and x cannot be attributed to ordering, because there is no direct evidence of different activation energies for diffusion in the ordered and disordered alloy in L1₂ ordering, which implies that neither the formation nor the migration energies for vacancies are affected by the degree of order [241]. A possible explanation comes then from the following considerations: First of all mechanical milling induces a substantial quantity of excess point and line defects. Then this high concentration of excess points defects, mainly vacancies and antisites assists diffusive processes and tends to be eliminated upon annealing. Finally, contamination of the Ni₃Al-based powders during milling process is unavoidable. The grinding impurities (in solid solution) can act as obstacles to defect migration, affecting in this way the observed kinetics.

7.6. Conclusions

The reordering of mechanically disordered Ni₃Al-based alloys was experimentally studied by means

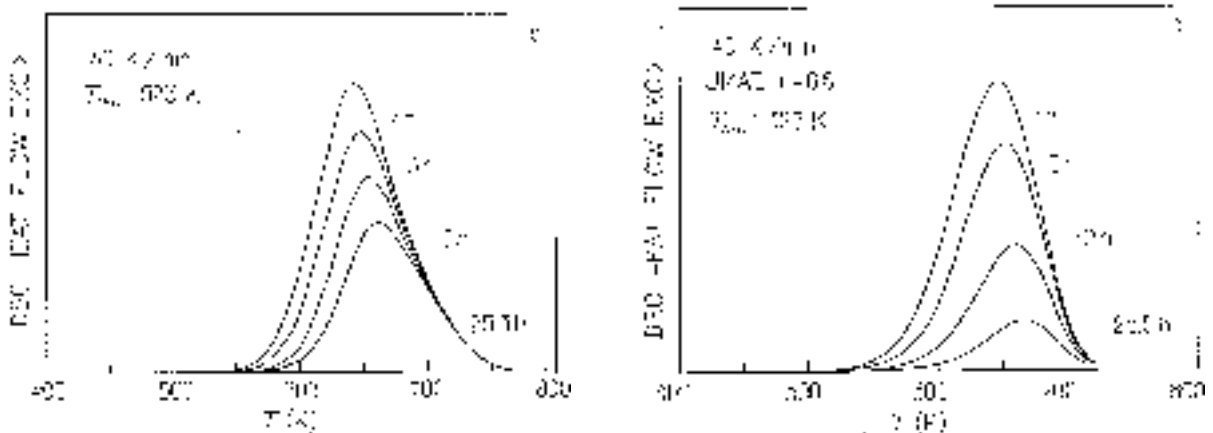


Fig.7.10. a) Continuous heating curves obtained after different isothermal annealing at 523K for one of the samples analyzed. The third contribution is subtracted and only the second contribution to the DSC peak is shown. b) Simulation of the continuous heating curves shown in a) according to the JMAE model. The following parameters have been used: $E= 1.6$ eV, $k_0= 3 \cdot 10^{10}$ and $p=0.6$.

of differential scanning calorimetry and magnetization measurements.

The apparent activation energies of the second stage are very close to the reported values of the activation energies for ordering and vacancy migration in these alloys. Reordering occurs through the formation and coarsening of ordered domains.

The JMAE analysis applied to the reordering transformation gives low values of the kinetic exponent (in the range of 0.6-1). These can be explained by assuming a model in which order cannot propagate from grain to grain [235].

However, in order to correctly reproduce both calorimetric and magnetic results obtained upon isothermal annealing, an increasing value for the apparent activation energy of the process is needed. This variation of the apparent activation energy with the temperature and the degree of transformation cannot be attributed to ordering. It seems the increase in activation energy with increasing annealing temperature can be explained in the frame of a model of vacancy annealing in presence of impurities.

8. CONCLUDING REMARKS

Methods of the severe plastic deformation (SePD) such as equal channel angular pressing and high-pressure torsion serve as a unique method for synthesizing nanostructured materials for not only scientific interests but also for potentials of industrial applications. Nanostructured metals and alloys possess some unique physical and mechanical properties differ from those of their coarse-grained counterparts due to high density of severe-deformation-induced non-homogeneities in the interfacial structures as well as presence of high-density ensembles of lattice defects.

For ECAP processing there is a high sensibility of plastic deformation uniformity to friction conditions between ingot and die. The approaches of enhancement of ECA pressing uniformity due to optimization of friction conditions based on the obtained results of experimental and FEM have allowed to fabricate bulk ingots with uniform nanostructured states in hard-to-deform tungsten and titanium. The grain growth kinetics in ultrafine-grained nickel processed by ECAP is controlled by grain boundary diffusion and possibly by other short-circuit diffusion paths that may exist in nanostructured materials. The temperature onset of grain growth is relatively low for normal grain growth but it is consistent with the decrease in thermal stability observed in ultrafine-grained metals processed by severe plastic deformation. The results demonstrate

a good correlation between the microhardness measurements and microstructural observations following ECAP and annealing.

For HPT deformation it was established that samples processed with more than ~ 5 turns are capable of producing reasonably homogeneous microstructures. An additional important processing parameter is the applied pressure. The experimental results show that higher pressures facilitate the formation of ultrafine-grained microstructures.

It is an established fact that metals and alloys subjected to preliminary deformation have somewhat higher diffusivities along grain boundaries (generally by an order of magnitude) relative to their counterparts subjected to recrystallization. The method of severe plastic deformation allows one to attain high levels of deformation and high density of defects in both grain volume and on the grain boundaries. At the same time, the observed increase in grain boundary diffusivity by at least four orders of magnitude has to be verified experimentally with the aid of various techniques.

Thus, there are controversial experimental data and theoretical representations on diffusion processes in nanostructured materials. At the same time, diffusion in mechanically synthesized bulk nanostructured materials is definitely recognized as the strongly enhanced diffusion compared to that in coarse-grained polycrystals and nanocrystalline materials fabricated by non-mechanical (more equilibrium than mechanical) methods. This experimentally documented phenomenon is naturally explained as that occurring due to the deformation-induced non-equilibrium state of grain boundaries, in which case mechanically generated grain boundary defects strongly enhance the boundary diffusivity.

We suppose for the first time that the HSRs phenomenon can be explained by the existence of the equilibrium GB liquid-like layer close to the bulk solidus.

The reordering of mechanically disordered Ni₃Al-based alloys was experimentally studied by means of differential scanning calorimetry and magnetization measurements. The apparent activation energies are very close to the the activation energies for ordering and vacancy migration in these alloys. Reordering occurs through the formation and coarsening of ordered domains. However, in order to correctly reproduce both calorimetric and magnetic results obtained upon isothermal annealing, an increasing value for the apparent activation energy of the process is needed. This variation of the apparent activation energy with the temperature and the degree of transformation cannot be attributed to

ordering. It seems the increase in activation energy with increasing annealing temperature can be explained in the frame of a model of vacancy annealing in presence of impurities.

ACKNOWLEDGMENTS.

All authors acknowledge the financial support of the INTAS program (under contract 99-1216). This work was partially supported by DGR of Generalitat of Catalonia (A.P. Zhilyaev), by Deutsche Forschungsgemeinschaft under projects Scha428/25-1 and 30-1 (H.-E. Schaefer and K. Reimann), by the Office of US Naval Research under Grant N00014-01-1-1020 (I. A. Ovid'ko), Volkswagen Foundation under project 05019225 (I. A. Ovid'ko), NATO Scientific Affairs Division under Grant PST.CLG977712 (I. A. Ovid'ko and A.B. Reizis), Russian Foundation of Basic Research under Grants 01-02-16853 (I. A. Ovid'ko and A. B. Reizis), 01-02-97039 and 01-02-16473 (B. B. Straumal), German Federal Ministry for Education and Research under WTZ-project RUS 00/209 (B. B. Straumal), Universitat de Valencia (B. B. Straumal) and NATO Science for Peace Programme under project 977997 (B. B. Straumal).

REFERENCES

- [1] H. Gleiter // *Prog. Mater. Sci.* **33** (1989) 223.
- [2] R.Z. Valiev // *Ann. Chimie* **21** (1991) 369.
- [3] S.X. McFadden, R.S. Mishra, R.Z. Valiev, A.P. Zhilyaev and A.K. Mukherjee // *Nature* **398** (1999) 684.
- [4] Yu.R. Kolobov, *Diffusion-controlled processes in grain boundaries and plasticity of metallic polycrystals* (Nauka, Novosibirsk, 1998), in Russian.
- [5] H.-E. Schaefer, In: *Mechanical Properties and Deformation Behavior of Materials Having Ultra-Fine Microstructures*, ed. by M. Nastasi et al. (Kluwer, Academic Publishers, 1993), p. 81.
- [6] R.Z. Valiev, A.V. Korsnikov and R.R. Mulyukov // *Mater. Sci. Eng. A* **166** (1993) 141.
- [7] R.Z. Valiev // *Mater. Sci. Forum.* **243-245** (1997) 207.
- [8] I.A. Ovid'ko // *Rev. Adv Mater. Sci.* **1** (2000) 61.
- [9] I.A. Ovid'ko, In: *Nanostructured Films and Coatings*, ed. by G-M. Chow, I.A. Ovid'ko and T.Tsakalagos (Kluwer, Dordrecht, 2000) p. 231.
- [10] T.C. Lowe and R.Z. Valiev (eds.), *Investigations and Applications of Severe Plastic Deformation*. (Kluwer, Dordrecht, 2000), p. 394.
- [11] R.Z. Valiev, I.V. Alexandrov and R.K. Islamgaliev, In: *Nanocrystalline Materials: Science and Technology*, ed. by G. M. Chow and N. I. Noskova (Kluwer, Dordrecht, 1998), p. 121.
- [12] R.Z. Valiev, O.A. Kaibyshev, R.I. Kuznetsov, R.Sh. Musalimov and N.K. Tsenev // *DAN SSSR* **301** (1988) 864, in Russian.
- [13] R.Z. Valiev, N.A. Krasilnikov and N.K. Tsenev // *Mater. Sci. Eng. A* **137** (1991) 35.
- [14] R.Z. Valiev and R.K. Islamgaliev, In: *Superplasticity and Superplastic Forming*, ed. by A.K. Ghosh and T.R. Bieler (MMMS, Warrendale, 1998), p.117.
- [15] R.Z. Valiev and R.K. Islamgaliev // *Fiz. Met. Metalloved.* **85 (3)** (1998) 161, in Russian.
- [16] R.Z. Valiev // *Nanostruct. Mater.* **6** (1995) 73.
- [17] N.A. Smirnova, V.I. Levit, V.I. Pilyugin, R.I. Kuznetsov, L.S. Davydova and V.A. Sazonova // *Fiz. Met. Metalloved.* **61** (1986) 1170, in Russian.
- [18] N.A. Smirnova, V.I. Levit, V.I. Pilyugin, R.I. Kuznetsov and M.V. Degtyarov // *Fiz. Met. Metalloved.* **62** (1986) 566, in Russian.
- [19] N.A. Smirnova, V.I. Levit and M.V. Degtyarov // *Fiz. Met. Metalloved.* **65** (1988) 1198, in Russian.
- [20] R.Z. Valiev, Yu.V. Ivanisenko, E.F. Rauch and B. Baudalet // *Acta Mater.* **44** (1997) 4705.
- [21] R.Z. Valiev, In: *Synthesis and processing of nanocrystalline powder*, ed. by D.L. Bourell (MMMS, Warrendale, 1996), p.153.
- [22] I.V. Alexandrov, Y.T. Zhu, T.C. Lowe, R.K. Islamgaliev and R.Z. Valiev // *Nanostruct. Mater.* **10** (1998) 49.
- [23] I.V. Alexandrov, Y.Zhu, T. Lowe, R.K. Islamgaliev and R.Z. Valiev // *Metall. Mater. Trans.* **29A** (1998) 2253.
- [24] V.M. Segal, V.I. Reznikov, A.E. Drobyshevskij and V.I. Kopylov // *Metally* **1** (1981) 115, in Russian.
- [25] Y. Iwahashi, J. Wang, Z. Horita, M. Nemoto and T.G. Langdon // *Scripta Mater.* **35**, (1996) 143.
- [26] V.M. Segal // *Mater. Sci. Eng. A* **197** (1995) 157.
- [27] V.M. Segal, V.I. Reznikov, V.I. Kopylov, D.A. Pavlik and V.F. Malyshev. In: *Processes of plastic transformation of metals* (Navuka i tehnika, Minsk (1984), p.295, in Russian.

- [28] Y. Iwahashi, Z. Horita, M. Nemoto and T.G. Langdon // *Acta Mater.* **46** (1998) 1589.
- [29] S. Ferrase, V.M. Segal, K.T. Hartwig and R.E. Goforth // *Metall. Mater. Trans.* **28A** (1997) 1047.
- [30] Y. Iwahashi, Z. Horita, M. Nemoto and T.G. Langdon // *Acta Mater.* **45** (1997) 4733.
- [31] N.H. Ahmadeev, R.Z. Valiev, V.I. Kopylov and R.R. Mulyukov // *Russian Metallurgy* **5** (1992) 96, in Russian.
- [32] O.R. Valiahmetov, R.M. Galeev and G.A. Salishchev // *Fiz. Metall. Metalloved.* **70(10)** (1990) 204, in Russian.
- [33] R.M. Galeev, O.R. Valiahmetov and G.A. Salishchev // *Russian Metallurgy* **4** (1990) 97, in Russian.
- [34] R.M. Imayev, V.M. Imayev and G.A. Salishchev // *J. Mater. Sci.* **27** (1992) 4465.
- [35] G.A. Salishchev, O.R. Valiakhmetov and R.M. Galeev // *J. Mater. Sci.* **28** (1993) 2898.
- [36] O. Kaibyshev, R. Kaibyshev and G. Salishchev // *Mater. Sci. Forum* **113-115** (1993) 423.
- [37] V.A. Valitov, G.A. Salishchev and Sh.H. Muhtarov // *Russian Metallurgy* **3** (1994) 127, in Russian.
- [38] G.A. Salishchev, O.R. Valiakhmetov, V.A. Valitov and S.K. Mukhtarov // *Mater. Sci. Forum* **170-172** (1994) 121.
- [39] G.A. Salishchev, O.R. Valiahmetov, R.M. Galeev and S.P. Malysheva // *Russian Metallurgy* **4** (1996) 86, in Russian.
- [40] R.Z. Valiev, R.K. Islamgaliev and I.V. Alexandrov // *Prog. Mater. Sci.* **45** (2000) 103.
- [41] K. Oh-ishi, Z. Horita, M. Furukawa, M. Nemoto and T.G. Langdon // *Metall. Mater. Trans. A* **29** (1998) 2011.
- [42] V.S. Zhernakov, I.N. Budilov, G.I. Raab, I.V. Alexandrov and R.Z. Valiev // *Scripta Mater.* (2001), in press.
- [43] ANSYS 5.5. License N: 0963.
- [44] V.A. Zhorin, D.P. Shashkin and N.S. Yenikopyan // *DAN SSSR* **278** (1984) 144, in Russian.
- [45] R.I. Kuznetsov, V.I. Bykov, V.P. Chernyshov, V.P. Pilyugin, N.A. Yefremov and V.V. Posheye, *Plastic deformation of solid bodies under pressure* (IFM UNTS AN USSR, Sverdlovsk 1985), Preprint 4/85, in Russian.
- [46] J. Bridgman, *Processing of metals under high pressure conditions* (Techizdat, Moscow, 1936), Russian translation.
- [47] R.Z. Valiev, R.S. Mishra, J. Grosa and A.K. Mukherjee // *Scripta Mater.* **34** (1996) 1443.
- [48] H. Shen, Z. Li, B. Günther, A.V. Korznikov and R.Z. Valiev // *Nanostructured Mater.* **6** (1995) 385.
- [49] R.K. Islamgaliev, F. Chmelik and R. Kuzel // *Mat. Sci. Eng. A* **237** (1997) 43.
- [50] N.M. Amirkhanov, R.K. Islamgaliev, R.Z. Valiev. In: *Nanostructured Materials*, ed. by N.I. Noskova and G.G. Taluts (URO RAN, Ekaterinburg, 1999), p. 333.
- [51] A.V. Korznikov, G.F. Korznikova, M.M. Myshlyayev, R.Z. Valiev, D.A. Salimonenko and O. Dimitrov // *Fiz. Met. Metall.* **84(4)** (1997) 413, in Russian.
- [52] A.P. Zhilyaev, S. Lee, G.V. Nurislamova, R.Z. Valiev and T.G. Langdon. // *Scripta Mater.* (2001), in press.
- [53] Z. Horita, D.J. Smith, M. Nemoto, R.Z. Valiev and T.G. Langdon // *J. Mater. Res.* **13** (1998) 446.
- [54] J. Philibert, *Atom Movement, Diffusion and Mass Transportation in Solids* (Editions de Physique, Les Ulis, 1991).
- [55] A.V. Korznikov, Yu.I. Ivanisenko, D.V. Laptionok, I.M. Safarov, V.P. Pilyugin and R.Z. Valiev // *Nanostruct. Mater.* **4** (1994) 159.
- [56] J. Languillaume, F. Chmelik, G. Kapelski, F. Bordeaux, A.A. Nazarov, G. Canova, C. Esling, R.Z. Valiev and B. Baudelet // *Acta Met. Mater.* **41** (1993) 2953.
- [57] A. Korznikov, O. Dimitrov, A. Ouivy, G. Korznikova, J. Devaud and R. Valiev // *J. de Phys. IV. Coll.* **5** (1995) C7-271.
- [58] A. Korznikov, O. Dimitrov and G. Korznikova // *Ann. Chim. Fr.* **21** (1996) 443.
- [59] Kh.Ya. Mulyukov, G.F. Korznikova, R.Z. Abdulov and R.Z. Valiev // *JMMM* **89** (1990) 207.
- [60] Kh.Ya. Mulyukov, G.F. Korznikova and R.Z. Valiev // *Phys. Stat. Sol. (a)* **125** (1991) 609.
- [61] H. Chen, Li Z, B. Guenter, A.V. Korznikov and R.Z. Valiev // *Nanostruct. Mater.* **6** (1995) 215.
- [62] R.K. Islamgaliev, R.Ya. Murtazin, L.A. Syutina and R.Z. Valiev // *Phys. Stat. Sol. (a)* **129** (1992) 231.
- [63] V.Yu. Gertsman, R. Birringer, R.Z. Valiev and H. Gleiter // *Scripta Metal Mater.* **30** (1994) 229.
- [64] A.P. Zhilyaev, G.V. Nurislamova, M.D. Baró, R.Z. Valiev and T.G. Langdon // *Scripta Mater.* (2001), in press.

- [65] J. Lian, R.Z. Valiev and B. Baudalet // *Acta Mater.* **43** (1995), 4165.
- [66] A.R. Wazzan // *J. Appl. Phys.* **36** (1965) 3596.
- [67] N. Wang, Z. Wang, K.T. Aust and U. Erb // *Acta Mater.* **45** (1997) 1655.
- [68] M.C. Lordache, S.H. Whang, Z. Jiao, Z.M. Wang // *Nanostr. Mater.* **11** (1999) 1345.
- [69] H. Gleiter // *Physica status solidi. (b)* **172** (1992) 41.
- [70] H.J. Hoefler and R.S. Averbach and H. Gleiter // *Phil. Mag. Letts.* **68** (1993) 99.
- [71] S.M. Klotsman // *Fiz. Met. Metalloved.* **75(4)** (1993) 5, in Russian.
- [72] L.N. Larikov // *Metal. Phys. Appl. Tech.* **17** (1995) 1.
- [73] B.S. Bokstein, H.D. Brose, L.I. Trusov and T.P. Khvostantseva // *Nanostruct. mater.* **6** (1995) 873.
- [74] S.V. Divinski and L.N. Larikov // *Defect Diff. Forum* **143-147** (1997) 1469.
- [75] R. Würschum, K. Reimann, S. Grub, A. Kubler, P. Scharwaechter, W. Frank, O. Kruse, H.D. Carstanjen and H.-E. Schaefer // *Phil. Mag. B* **76** (1997) 407.
- [76] H. Tanimoto, P. Farber, R. Würschum, R.Z. Valiev and H.-E. Schaefer // *Nanostruct. Mater.* **12** (1999) 681.
- [77] H. Tanimoto, L. Pasquini, R. Prummer, H. Kronmüller and H.-E. Schaefer // *Scripta Mater.* **42** (2000) 961.
- [78] H.-E. Schaefer, K. Reimann, W. Straub, F. Phillipp, H. Tanimoto, U. Brossmann and R. Wurschum // *Mat. Sci. Eng., A* **286** (2000) 24.
- [79] P. Keblinski, D. Wolf, S.R. Phillpot and H. Gleiter // *Scripta Mater.* **41** (1999) 631.
- [80] R. Wurschum, A. Kubler, S. Gruss, P. Scharwaechter, W. Frank, R.Z. Valiev, R.R. Mulyukov and H.-E. Schaefer // *Ann. Chimie* **21** (1996) 471.
- [81] H.-E. Schaefer, R. Wurschum, T. Gessmann, G. Stockl, P. Scharwaechter, W. Frank, R.Z. Valiev, H.-J. Fecht and C. Moelle // *Nanostruct. Mater.* **6** (1995) 869.
- [82] Yu.R. Kolobov, G.P. Grabovetskaya, I.V. Ratochka, E.V. Kabanova, E.V. Naidenkin and T.C. Lowe // *Ann. Chimie* **21** (1996) 483.
- [83] G.P. Grabovetskaya, I.V. Ratochka, Yu.R. Kolobov and L.N. Puchkareva // *The Phys. Met. Metalloved.* **83(3)** (1997) 310, in Russian.
- [84] Yu.R. Kolobov, G.P. Grabovetskaya, M.B. Ivanov, A.P. Zhilyaev and R.Z. Valiev // *Scripta Mater.* **44** (2001) 873.
- [85] I. Kaur, Yu. Mishin and W. Gust, *Fundamentals of Grain and Interphase Boundary Diffusion* (John Wiley, Chichester, 1995).
- [86] L.G. Kornelyuk, A.Yu. Lozovoi and I.M. Razumovskii // *Def. Diff. Forum* **143-147** (1997) 1481.
- [87] U. Brossmann, R. Würschum, U. Södervall and H.-E. Schaefer // *J. Appl. Phys.* **85** (1999) 7646.
- [88] R. Würschum, E. Shapiro, R. Dittmar and H.-E. Schaefer // *Phys. Rev. B* **62** (2000) 12021.
- [89] R. Würschum, K. Reimann, S. Grub, A. Kübler, P. Scharwaechter, W. Frank, O. Kruse, H. D. Carstanjen and H.-E. Schaefer // *Phil. Mag. B* **76** (1997) 407.
- [90] K. Reimann, H.-J. Fecht and H.-E. Schaefer // *Scripta Mater.* **44** (2001) 1999.
- [91] A. Gude and H. Mehrer // *Phil. Mag. A* **76** (1997) 1.
- [92] M. Eggersmann and H. Mehrer // *Phil. Mag. A* **80** (2000) 1219.
- [93] S. Frank, S.V. Divinski, U. Södervall and C. Herzig // *Acta Mater.* **49** (2001) 1399.
- [94] L. Pasquini, A. A. Rempel, R. Würschum, K. Reimann, M. Müller, B. Fultz and H.-E. Schaefer // *Phys. Rev. B* **63** (2001) 134114.
- [95] H.-E. Schaefer, K. Frenner and R. Würschum // *Intermetallics* **7** (1999) 277.
- [96] K. Reimann and H.-E. Schaefer, In: *Proc. of ICETS2000-ISAM, Vol. 2*, ed. by Jian Song and Ruiyu Yin (New World Press, Beijing, 2000), p. 1460.
- [97] H. Gleiter // *Nanostruct. Mater.* **6** (1995) 3.
- [98] H. Gleiter // *Acta Mater.* **48** (2000) 1.
- [99] *Nanotechnology Research Directions*, ed. by M.Roco, R.S. Williams and P. Alivisatos (Kluwer, Dordrecht, 2000).
- [100] *Nanomaterials: Synthesis, Properties and Applications*, ed. by A.S. Edelstein and R.C. Cammarata (Inst. Phys. Publ., Bristol and Philadelphia, 1996).
- [101] *Nanostructured Materials: Science and Technology*, ed. by G.-M. Chow and N.I. Noskova (Kluwer, Dordrecht, 1998).
- [102] *R&D Status and Trends in Nanoparticles, Nanostructured Materials, and Nanodevices in the United States*, ed. by R.W. Siegel, E. Hu and M.C. Roco (International Technology Research Inst., Baltimore, 1998).

- [103] *Nanostructured Films and Coatings*, ed. by G.-M. Chow, I. A. Ovid'ko and T. Tsakalakos (Kluwer, Dordrecht, 2000).
- [104] *Russian R & D Activities on Nanoparticles and Nanostructured Materials*, ed. by I.A. Ovid'ko and M.C. Roco (International Technology Research Inst, Baltimore, 1998).
- [105] R.Z. Valiev and I.V. Alexandrov, *Nanostructured Materials Fabricated by Severe Plastic Deformation* (Moscow, Logos, 2000), in Russian.
- [106] M.Yu. Gutkin and I.A. Ovid'ko, *Defects and Plasticity Mechanisms in Nanostructured and Non-Crystalline Materials* (St. Petersburg, Yanus, 2001), in Russian.
- [107] J. Horvath, R. Birringer and H. Gleiter // *Solid State Comm.* **62** (1987) 391.
- [108] Yu.R. Kolobov, G.P. Grabovetskaya, I.V. Ratochka and K.V. Ivanov // *Nanostruct. Mater.* **12** (1999) 1127.
- [109] Yu.R. Kolobov, G.P. Grabovetskaya, K.V. Ivanov, R.Z. Valiev and T.C. Lowe, In: *Investigations and Applications of Severe Plastic Deformation*, ed. by T.C. Lowe and R.Z. Valiev (Kluwer, Dordrecht, 2000), p.261.
- [110] J.C. Fischer // *J. Appl. Phys.* **22** (1951) 74.
- [111] R.T.P. Whipple // *Phil.Mag.* **45** (1954) 122.
- [112] T. Suzuoka // *Trans. Jap. Inst. Metals* **2** (1961) 2.
- [113] P. Benoist and G. Martin // *Thin Solid Films* **25** (1975) 181.
- [114] G. Harrison // *Trans. Faraday Soc.* **57** (1961) 1191.
- [115] B.S. Bokshtein, *Diffusion in Metals* (Moscow, Metallurgiya, 1978), in Russian.
- [116] V.T. Borisov, V.M. Golikov and G.V. Shcherbedinskii // *Fiz. Met. Metalloved.* **17** (1964) 881, in Russian.
- [117] R.W. Balluffi, T. Kwok, P.D. Bristowe et al. // *Scripta Metall.* **15** (1981) 951.
- [118] P.D. Bristowe, A. Brokman, T. Spaepen and R.W. Balluffi // *Sripta Metall.* **14** (1980) 943.
- [119] A. Brokman, P.D. Bristowe, R.W. Balluffi et al. // *Appl. Phys.* **52** (1981) 6116.
- [120] T. Kwok, P.S. Ho, S. Yip, R.W. Balluffi et al. // *Phys. Rev. Lett.* **47** (1981) 1148.
- [121] L.M. Klinger and D.A. Gorbunov, *Structure and Properties of Interfaces in Metals* (Moscow, Nauka, 1988), in Russian.
- [122] Q. Ma and R.W. Balluffi // *Acta Metall. Mater.* **42** (1994) 1.
- [123] A.P. Sutton and R.W. Balluffi, *Interfaces in Crystalline Materials* (Oxford. Science Publications, Oxford, 1996).
- [124] R.Z. Valiev, V. Yu. Gertsman and O.A. Kaibyshev // *Phys. Stat. Sol. (a)* **61** (1980) K9.
- [125] P.H. Pumphrey and H. Gleiter // *Phil. Mag.* **30** (1974) 593.
- [126] A.A. Nazarov, A.E. Romanov and R.Z. Valiev // *Scripta Metall. Mater.* **24** (1990) 1929.
- [127] A.A. Nazarov // *Ann. Chimie* **21** (1996) 461.
- [128] A.A. Nazarov // *Mater. Sci. Forum* **243-245** (1997) 31.
- [129] A.V. Osipov and I.A. Ovid'ko // *Appl. Phys.A* **54** (1992) 517.
- [130] I.A. Ovid'ko and A.B. Reizis // *J.Phys.D* **32** (1999) 2833.
- [131] E.S. Smirnova and V.N. Chuvil'deev // *Fiz. Met. Metalloved.* **88(1)** (1999) 74, in Russian.
- [132] H.J. Hofer, H. Hahn and S. Averbach // *Defect Diff. Forum* **68** (1993) 99.
- [133] Yu. Mishin and Ch. Herzig // *Nanostruct. Mater.* **6** (1995) 859.
- [134] V.B. Rabukhin and A.S. Panikarskii // *Poverkhnost* **5(5)** (1986) 150, in Russian.
- [135] V.B. Rabukhin // *Poverkhnost* **5(7)** (1986) 126, in Russian.
- [136] G. Palumbo and K.T. Aust // *Mater. Sci. Eng. A* **113** (1989) 139.
- [137] K.M. Yin, A.H. King, T.E. Hsieh, F.R. Chen, J.J. Kai and L. Chang // *Microsc. Microanal.* **3** (1997) 417.
- [138] U. Czubayko, V.G. Sursaeva, G. Gottstein and L.S. Shvindlerman, In: *Grain Growth in Polycrystalline Materials III*, ed. by H. Weiland, B.L. Adams and A.D. Rollett (Pittsburg, TMS, 1998), p. 423.
- [139] A.H. King // *Interf. Sci.* **7** (1999) 251.
- [140] V.I. Vladimirov, *Einführung in die Physikalische Theorie der Plastizität and Festigkeit* (VEB Deutscher Verlag für Grundstoffindustrie, Leipzig, 1975).
- [141] R.A. Masumura and I.A. Ovid'ko // *Mater. Phys. Mech.* **1** (2000) 31.
- [142] A. A. Nazarov // *Phil. Mag. Lett.* **80** (2000) 221.
- [143] I.A. Ovid'ko, A.B. Reizis and R.A. Masumura // *Mater. Phys. Mech.* **1** (2000) 103.
- [144] I.A. Ovid'ko and A.B. Reizis // *Phys. Sol. State* **43** (2001) 35.
- [145] J.P. Hirth and J.Lothe, *Theory of Dislocations* (Mc Graw-Hill, NewYork, 1968).

- [146] L.A. Girifalco and D.O. Welch, *Point Defects and Diffusion in Strained Metal* (Gordon and Breach, New-York, 1967).
- [147] V.G. Gryaznov and L.I. Trusov // *Progr. Mater. Sci.* **37** (1993) 289.
- [148] I.A. Ovid'ko and A.G. Sheinerman, paper under preparation.
- [149] J.H. van der Merve // *Crit. Rev. Sol. State Mater. Sci.* **17** (1991) 187.
- [150] E.A. Fitzgerald // *Mater. Sci. Rep.* **7** (1991) 87.
- [151] A. Robert and C. Kiely // *Phys. Rev. B* **44** (1991) 1154.
- [152] S.C. Jain, A.H. Harker and R.A. Cowley // *Phil. Mag. A* **75** (1997) 1461.
- [153] J.P. Hirth // *Acta Mater.* **48** (2000) 93.
- [154] F. Spaepen // *Acta Mater.* **48** (2000) 31.
- [155] I.A. Ovid'ko // *J. Phys.: Cond. Matter* **11** (1999) 6521.
- [156] M.Yu. Gutkin, I.A. Ovid'ko and A.G. Sheinerman // *J. Phys.: Cond. Matter* **12** (2000) 5391.
- [157] I.A. Ovid'ko // *J. Phys.: Cond. Matter* **13** (2001) L97.
- [158] T.G. Langdon, T. Watanabe, J. Wadsworth, M.J. Mayo, S.R. Nutt and M.E. Kassner // *Mater. Sci. Eng. A* **166** (1993) 237.
- [159] B.B. Straumal and W. Gust // *Mater. Sci. Forum* **207–209** (1996) 59.
- [160] B. Straumal, D. Molodov and W. Gust // *J. Phase Equilibria* **15** (1994) 386.
- [161] B. Straumal, T. Muschik, W. Gust and B. Predel // *Acta Metall. Mater.* **40** (1992) 939.
- [162] L.-S. Chang, E. Rabkin, B.B. Straumal, S. Hofmann, B. Baretzky and W. Gust // *Defect Diff. Forum* **156** (1998) 135.
- [163] B. Straumal, V. Semenov, V. Glebovsky and W. Gust // *Defect Diff. Forum* **143–147** (1997) 1517.
- [164] B. B. Straumal, W. Gust and T. Watanabe // *Mater. Sci. Forum* **294–296** (1999) 411.
- [165] B. Straumal, W. Gust and D. Molodov // *Interface Sci.* **3** (1995) 127.
- [166] B. Straumal and D. Molodov, W. Gust // *Mater. Sci. Forum* **207–209** (1996) 437.
- [167] B. Straumal, S. Risser, V. Sursaeva, B. Chenal and W. Gust // *J. Physique IV* **5-C7** (1995) 233.
- [168] D.A. Molodov, U. Czubyko, G. Gottstein, L.S. Shvindlerman, B.B. Straumal and W. Gust // *Phil. Mag. Lett.* **72** (1995) 361.
- [169] L.-S. Chang, B.B. Straumal, E. Rabkin, W. Gust and F. Sommer // *J. Phase Equilibria* **18** (1997) 128.
- [170] L.-S. Chang, E. Rabkin, B. Straumal, P. Lejcek, S. Hofmann and W. Gust // *Scripta Mater.* **37** (1997) 729.
- [171] E.I. Rabkin, V.N. Semenov, L.S. Shvindlerman and B.B. Straumal // *Acta Metall. Mater.* **39** (1991) 627.
- [172] O.I. Noskovich, E.I. Rabkin, V.N. Semenov, L.S. Shvindlerman and B.B. Straumal // *Acta Metall. Mater.* **39** (1991) 3091.
- [173] B.B. Straumal, O.I. Noskovich, V.N. Semenov, L.S. Shvindlerman, W. Gust and B. Predel // *Acta Metall. Mater.* **40** (1992) 795.
- [174] B. Straumal, E. Rabkin, W. Lojkowski, W. Gust and L.S. Shvindlerman // *Acta Mater.* **45** (1997) 1931.
- [175] E. Rabkin, D. Weygand, B. Straumal, V. Semenov, W. Gust and Y. Bréchet // *Phil. Mag. Lett.* **73** (1996) 187.
- [176] V.G. Glebovsky, B.B. Straumal, V.N. Semenov, V.G. Sursaeva and W. Gust // *High Temp. Mater. Proc.* **13** (1994) 67.
- [177] M.C. Flemings // *Metall. Trans. A* **22** (1991) 957.
- [178] P. Kumar, C.L. Martin, and S. Brown // *Metall. Trans. A* **24** (1993) 110.
- [179] C. P. Chen and C.-Y.A. Tsao // *Acta Mater.* **45** (1997) 1955.
- [180] M.C. Roth, G.C. Weatherly, and W.A. Miller // *Acta Metall.* **28** (1980) 841.
- [181] B.L. Vaandrager and G.M. Pharr // *Acta Metall.* **37** (1989) 1057.
- [182] B. Baudelet, M.C. Dang and F. Bordeaux // *Scripta Metall. Mater.* **32** (1995) 707.
- [183] H. Iwasaki, T. Mori, M. Mabuchi, K. Higashi // *Acta Mater.* **46** (1998) 6351.
- [184] G.M. Pharr, P.S. Godavarti and B.L. Vaandrager // *J. Mater. Sci.* **24** (1989) 784.
- [185] *Binary Alloy Phase Diagrams*, ed. T.B. Massalski et al. (ASM International, Materials Park OH, 1993) p. 170 and 240.
- [186] J.W. Cahn // *J. Phys. Colloq.* **43-C6** (1982) 199.
- [187] D. Weygand, Y. Bréchet, E. Rabkin, B. Straumal and W. Gust // *Phil. Mag. Lett.* **76** (1997) 133.
- [188] K. Higashi, S. Tanimura and T. Ito // *MRS Proc.* **196** (1990) 385.

- [189] T. Imai, M. Mabuchi, Y. Tozawa and M. Yamada // *J. Mater. Sci. Lett.* **2** (1990) 255.
- [190] M. Mabuchi and T. Imai // *J. Mater. Sci. Lett.* **9** (1990) 763.
- [191] T.G. Nieh, C.A. Henshall and J. Wadsworth // *Scripta Metall.* **18** (1984) 1405.
- [192] M. Mabuchi, K. Higashi, Y. Okada, S. Tanimura, T. Imai and K. Kubo // *Scripta Metall.* **25** (1991) 2003.
- [193] T.G. Nieh, P.S. Gilman and J. Wadsworth // *Scripta Metall.* **19** (1985) 1375.
- [194] T.R. Bieler, T.G. Nieh and J. Wadsworth, A.K. Mukherjee // *Scripta Metall.* **22** (1988) 81.
- [195] K. Higashi, Y. Okada, T. Mukai and S. Tanimura // *Scripta Metall.* **25** (1991) 2053.
- [196] Y. Takayama, T. Tozawa and H. Kato // *Acta Mater.* **47** (1999) 1263.
- [197] K. Higashi, T.G. Nieh, M. Mabuchi and J. Wadsworth // *Scripta Metall. Mater.* **32** (1995) 1079.
- [198] T. Imai, M. Mabuchi, Y. Tozawa, Y. Murase and J. Kusui, In: *Metal & Ceramic Matrix Composites: Processing, Modeling & Mechanical Behavior*, ed. R.B. Bhagat et al. (TMS-AIME, Warrendale, 1990), p. 235.
- [199] M. Mabuchi, K. Higashi, T. Imai and K. Kubo // *Scripta Metall.* **25** (1991) 1675.
- [200] N. Furushiro, S. Hori and Y. Miyake, In: *Proc. Int. Conf. Superplast. Adv. Mats (ICSAM-91)*, ed. by S. Hori et al. (Jap. Soc. Res. Superplast., 1991) p. 557.
- [201] M. Mabuchi, K. Higashi and T. Langdon // *Acta Metall. Mater.* **42** (1992) 1739.
- [202] M. Mabuchi, K. Higashi, S. Wada and S. Tanimura // *Scripta Metall.* **26** (1992) 1629.
- [203] T.G. Nieh and J. Wadsworth // *Scripta Metall.* **28** (1993) 1119.
- [204] M. Mabuchi, K. Higashi, K. Inoue and S. Tanimura // *Scripta Metall.* **26** (1992) 1839.
- [205] J. Koike, M. Mabuchi and K. Higashi // *Acta Metall. Mater.* **43** (1995) 199.
- [206] M. Mabuchi, K. Higashi, Y. Okada, S. Tanimura, T. Imai and K. Kubo // *Scripta Metall.* **25** (1991) 2517.
- [207] T. Hikosaka, T. Imai, T. G. Nieh and J. Wadsworth // *Scripta Metall.* **31** (1994) 1181.
- [208] R.B. Grishaber, R. S. Mishra and A. K. Mukherjee // *Mat. Sci. & Eng. A* **220** (1996) 78.
- [209] T.G. Nieh, D.R. Lesuer and C.K. Syn // *Scripta Metall. Mater.* **32** (1995) 707.
- [210] J.S. Benjamin // *Sci. Amer.* **234** (1976) 40.
- [211] P.S. Gilman and J.S. Benjamin // *Ann. Rev. Mater. Sci.* **11** (1983) 279.
- [212] C.C. Koch // *Ann. Rev. Mater. Sci.* **19** (1989) 121.
- [213] C.C. Koch, In: *Processing of Metals and Alloys*, ed. by R. W. Cahn. (VCH Verlagsgesellschaft, Weinheim, 1991), p. 193.
- [214] R.Z. Valiev, R.K. Islamgaliev and I.V. Alexandrov // *Prog. Mater. Sci.* **2** (2000) 102.
- [215] A. Revesz, *PhD thesis* (Budapest: Eotvos University, 2000).
- [216] K. Mitsui, Y. Mishima and T. Suzuki // *Acta Met.* **37** (1986) 3379.
- [217] R.W. Cahn, M. Takeyama, J.A. Horton and C.T. Liu // *J. Mater. Res.* **6** (1991) 57.
- [218] R.W. Cahn, In: *High Temperature Aluminides. and Intermetallics*, ed. by S.H. Whang, C.T. Liu, D.P. Pope and J.O. Stiegler (TMS, Warrendale, 1990), p. 245.
- [219] J.S.C. Jang and C.C. Koch // *J. Mater. Res.* **5** (1990) 498.
- [220] G.J.C. Carpenter and E.M. Shulson // *Scripta Met.* **15** (1981) 549.
- [221] H.C. Liu and T.E. Mitchell // *Acta Met.* **31** (1983) 863.
- [222] A.R. Yavari and B. Bochu // *Phil. Mag. A* **59** (1989) 697.
- [223] J. Malagelada, S. Suriñach, M.D. Baró, S. Gialancla and R.W. Cahn // *Mat. Sci. Forum.* **88-90** (1992) 497.
- [224] A.R. Yavari, P. Crespo, E. Pulido, A. Hernando, G. Fillion, P. Lethuillier, M.D. Baró and S. Suriñach, In: *Ordering and Disorder in Alloys*, ed. by A.R. Yavari (Elsevier, London, 1992), p. 12.
- [225] S. Gialancla, R.W. Cahn, J. Malagelada, S. Suriñach, M.D. Baró and A.R. Yavari, In: *Kinetics of Ordering Transformation in Metals*, ed. by H. Chen and V.K. Vasudevan (TMS, Warrendale, 1992), p. 161.
- [226] S. Suriñach, M.D. Baró, M.T. Clavaguera-Mora and N. Clavaguera // *J. Non-Cryst. Solids* **58** (1983) 209.

- [227] S.R. Harris, D.H. Pearson, C.M. Garland and B. Fultz // *J. Mater. Res.* **6** (1991) 2019.
- [228] R.Z. Valiev, S. Song, S.X. McFadden, A.K. Mukherjee and R.S. Mishra // *Phil Mag. A* **81** (2001) 25.
- [229] K.L. Breitbach and L.S. Chumbley // *Scripta Metal. Mater.* **25** (1991) 2553.
- [230] J. Eckert Holzer, C.E. Krill and W.L. Johnson // *J. Mater. Res.* **7** (1992) 1751.
- [231] J. Rupp and R. Birringer // *Phys. Rev. B* **36** (1987) 7888.
- [232] J.K. Okamoto, *TMS Student Paper Competition* (1991).
- [233] J. Eckert, J.C. Holzer, C.E. Krill and W.L. Johnson // *Mat. Sci. Forum* **88-90** (1992) 505.
- [234] A.R. Yavari // *Acta Metall. Mater.* **41** (1993) 212.
- [235] M.T. Clavaguera-Mora, S. Suriñach, M.D. Baró and N. Clavaguera // *J. Phys. D* **25** (1992) 803.
- [236] M.J. Avrami // *Chem. Phys.* **7** (1939) 1103; *ibid.* **8** (1940) 212; *ibid.* **9** (1941) 177.
- [237] J.W. Christian, *The Theory of Transformations in Metals and Alloys* (Pergamon, Oxford, 1975).
- [238] H.E. Kissinger // *Anal. Chem.* **29** (1957) 1702.
- [239] M.D. Baró, S. Suriñach, J. Malagelada, M.T. Clavaguera-Mora, S. Gialanella and R.W. Cahn // *Acta Metall Mater.* **41** (1993) 1065.
- [240] R.W. Cahn, In: *Phase Transitions in Condensed Systems*, ed. by G. Slade Cargil III, F. Spaepen and K.N. Tu (MRS, Pittsburgh, 1987), p. C85.